POLARRIS: A POLArimetric Radar Retrieval and Instrument Simulator

Toshi Matsui[1&2], Brenda Dolan[3], Steven A. Rutledge[3], Wei-Kuo Tao[1],
Takamichi Iguchi[1&2], Julie Barnum[3], and Stephen Lang[1&4]

[1] *NASA Goddard Space Flight Center, Greenbelt, MD*

[2] *Earth System Science Interdisciplinary Center, University of Maryland College Park, Maryland*

[3] *Department of Atmospheric Science, Colorado State University, CO*

[4] *Science Systems and Applications, Inc., Lanham, MD*

Revised for JGR

Corresponding Author:
Toshi Matsui
Code 612, NASA Goddard Space Flight Center
Greenbelt, MD 20771
Tell: 301-614-5658
Toshihisa.Matsui-1@nasa.gov

Abstract. This paper introduces a synthetic polarimetric radar simulator and retrieval package, POLArimetric Radar Retrieval and Instrument Simulator (POLARRIS), for evaluating cloud-resolving models (CRMs). POLARRIS is composed of forward (POLARRIS-f) and inverse (retrieval and diagnostic) components (iPOLARRIS) to generate not only polarimetric radar observables (Z_h, Z_{dr}, K_{dp}, ρ_{hv}) but also radar-consistent geophysical parameters such as hydrometeor identification (HID), vertical velocity, and rainfall rates retrieved from CRM data. To demonstrate its application and uncertainties, POLARRIS is applied to simulations of a mesoscale convective system over the Southern Great Plains on 23 May 2011, using the Weather Research and Forecasting model (WRF) with both spectral bin microphysics (SBM) and the Goddard single-moment bulk 4ICE microphysics. Statistical composites reveal a significant dependence of simulated polarimetric observables (Z_{dr}, K_{dp}) on the assumptions of the particle axis ratio (oblateness) and orientation angle distributions. The simulated polarimetric variables differ considerably between the SBM and 4ICE microphysics in part due to the differences in their ice particle size distributions as revealed by comparisons with aircraft measurements. Regardless of these uncertainties, simulated HID distributions overestimates graupel and hail fractions, especially from the simulation with SBM. To minimize uncertainties in forward model, the particle shape and orientation angle distributions of frozen particles should be predicted in a microphysics scheme in addition to the size distributions and particle densities.

1. Introduction

Cloud-resolving models (CRMs) have been and will continue to be important tools in the weather and climate research community [e.g., *Tao and Moncrieff* 2009]. Consequently, establishment of robust frameworks to evaluate their dynamical and microphysical outputs is critical [e.g., *Jung et al.* 2010; *Fridlind et al.* 2012]. Ground and aircraft-based *in-situ* and remote sensing measurements are a vital source of validation for the microphysics and vertical velocities in CRMs [e.g., *Iguchi et al.* 2012b,c, 2014]. Indeed, reflectivity and Doppler velocities from ground-based radar have been used for evaluating microphysical characteristics [e.g., *Lang et al. 2007, 2011, 2014; Iguchi et al. 2012a, 2014*]. In the last decade, the widespread emergence of polarimetric radars has provided the opportunity for additional metrics in addition to the radar reflectivity factor at horizontal polarization (Z_h) for evaluating CRMs, including differential reflectivity (Z_{dr}), linear-depolarization ratio (*LDR*), specific differential phase (K_{dp}), and co-polar correlation coefficient (ρ_{hv}) [e.g., *Ryzhkov et al.* 2011; *Putnam et al.* 2017; Snyder et al. 2017a,b].

Jung et al. [2008a] first applied a polarimetric radar simulator to ensemble convection-permitting forecast simulations and examined the impact of polarimetric radar assimilation using an ensemble Kalman filter [*Jung et al.* 2008b]. *Jung et al.* [2010] applied single- and double-moment microphysics to the polarimetric simulators to examine whether the bulk microphysics schemes could reproduce specific spatial structures of polarimetric radar signals from a supercell thunderstorm and found that the single-moment scheme could not reproduce a Z_{dr} arc, mid-level Z_{dr}, and ρ_{hv} rings due to its inability to simulate size sorting effects.

Dawson et al. [2014] investigated the low-level Z_{dr} signature in supercell forward flanks using CRM simulations and a polarimetric radar simulator. *Snyder et al.* [2017] applied a polarimetric radar simulator to a CRM supercell simulation with a triple-moment microphysics scheme. *Ryzhkov et al.* [2011] developed a polarimetric radar simulator for more complex microphysics: the Hebrew University Cloud Model (HUCM) with spectral-bin microphysics (SBM). These previous studies examined observed and simulated vertical cross-sections of polarimetric variables (Z_h, Z_{dr}, LDR, K_{dp}, ρ_{hv}) in addition to the associated size distributions of CRM hydrometeors to understand particular convective processes with a focus on deep convective clouds. However, this type of direct comparison is not straightforward, because of i) the dependence of polarimetric radar observables on radar elevation angle and other factors, ii) the need to better understand the different polarimetric radar observables by the CRM community, and iii) uncertainties in the microphysics, especially the axis ratio and orientation angle distributions as noted in this study.

Recently, robust hydrometeor identification (HID) algorithms have been more widely applied to polarimetric radars at X-, C- and S-band [e.g., *Straka et al.* 2000, *Park et al.* 2009; *Dolan and Rutledge* 2009; *Snyder et al.* 2010; *Bechini and Chandrasekar* 2015]. HID algorithms retrieve bulk hydrometeor classes for given ranges of polarimetric radar observables. These detailed HID retrievals have great potential for constraining four dimensional distributions of bulk hydrometeors and thus microphysical conversion processes in CRMs, which have been a long-standing uncertainty in the community since the first appearance of primitive cloud microphysics schemes, particularly for mixed- and ice-phases [*Lin et al.* 1983; *Rutledge and Hobbs* 1984].

Putnam et al. [2014] applied a polarimetric radar simulator to regional storm-scale forecasts to evaluate bulk double-moment microphysics schemes by examining polarimetric radar observables (Z_h, Z_{dr}, K_{dp}) and HID categories. In a follow-up study, *Putnam et al.* [2017] evaluated five different microphysics schemes. These studies demonstrated that the polarimetric observables and retrievals performed better in evaluating performance details of cloud microphysics from simple to complex schemes compared to traditional methods using only radar reflectivity data [e.g., *Lang et al.* 2007].

Along with HID algorithms, vertical velocity and precipitation retrievals from Doppler, polarimetric-radar measurements have been improved via more reasonable assumptions in size, density, and terminal fall velocity [*Dolan et al.* 2013]. Observed polarimetric datasets provide a significant opportunity to validate the performance of CRMs and in the long run, improve the microphysical, dynamical and life cycle simulation of convective systems.

Toward the goal of more comprehensive model evaluation, data assimilation, and polarimetric radar retrieval development, a systematic framework for a polarimetric simulator is required, including a fast and accurate forward model as well as a rigorous inverse component for linking polarimetric observables with retrieved geophysical parameters. This paper introduces a synthetic polarimetric radar simulator and inverse retrieval framework for evaluating the microphysics and dynamics in CRMs. The POLArimetric Radar Retrieval and Instrument Simulator (POLARRIS) is composed of a forward model (POLARRIS-f) based on rigorous Mueller matrix [*Vivekenandan et al.* 1991] and an inverse (retrieval and diagnostic) component (iPOLARRIS) based on the

Colorado State University (CSU) radar retrievals [e.g., *Dolan and Rutledge* 2009; *Dolan et al.* 2013].

The paper is intended to demonstrate the utility and uncertainties of POLARRIS in evaluating the microphysical structures of a simulated MCS in a holistic statistical sense using bulk and bin microphysics. The intent here is not to compare the specific performance of the model dynamics or microphysics schemes. In Section 2, the detailed methods and software components of POLARRIS are described. In Section 3, uncertainties in particle assumptions and their impact on estimating polarimetric observables are detailed as well as the different assumptions in polarimetric simulators that have already been developed and are available in the community. In Section 4, POLARRIS applications are demonstrated using regional CRM simulations for a mid-latitude continental convective event. A summary of the capabilities and future applications are given in Section 5.

2. Methods

2.1 **POLARRIS-f: forward model**

The forward component, i.e., POLARRIS-f, is built upon the Goddard Satellite Data Simulator Unit (G-SDSU), which features a generalized end-to-end multi-instrument satellite simulator designed for CRMs [*Matsui et al.* 2013, 2014]. The G-SDSU includes microwave, radar, visible-infrared, lidar, and broadband satellite simulators with a unified CRM input module. G-SDSU can be used to evaluate CRM simulations [*Matsui et al.* 2009, 2016; *Li et al.* 2010; *Shi et al.* 2010; *Han et al.* 2013;

Chern et al. 2016], conduct data assimilation [*Zhang et al.* 2017], and support current and future satellite missions [*Matsui et al.* 2013; *Kidd et al.* 2016; *Iguchi and Matsui* 2018].

In POLARRIS-f, both T-Matrix and Mueller-Matrix modules [*Vivekenandan et al.* 1991] are integrated following the physical principles in the G-SDSU software modules [*Matsui et al.* 2014]: i.e., physical consistency between the CRM and forward models, including microphysics assumptions and atmospheric conditions. The exceptions are the particle shape and orientation angles, which are typically not predicted by the model microphysics as discussed in the next section. In the T-matrix module, the single scattering matrix of axis-symmetric oblate hydrometeors are computed while the Mueller-Matrix is used to estimate radar observables from the T-Matrix single-scattering properties for a given radar elevation angle and the assumed particle orientation angle distributions. Details on calculating the 4×4 Mueller matrix are described in *Vivekenandan et al.* [1991]; the calculation of the effective dielectric constant is given in Appendix A.

2.1.1 Integration of the Mueller Scattering Matrix and Radar Observables

Once a single-particle 4×4 Mueller scattering matrix (S, mm^2) is generated (see the equations in *Vivekenandan et al.* [1991]), it is integrated over the particle size distributions (PSDs) for each species class in the model to derive a size-integrated 4×4 Mueller scattering matrix ($\mathrm{S}|_i$, mm^2/m^3):

$$\mathrm{S}|_i = \int S\, N(D) dD \qquad \text{Eq. 1}$$

where *i* represents each particular hydrometeor species, and *N(D)* represents the particle number density (m^{-4}) for a given particle diameter *D* (m). In typical bulk microphysics schemes with four ice categories such as the Goddard 4ICE scheme [*Lang et al.* 2014; *Tao et al.* 2016], the hydrometeor species are cloud, rain, ice crystals, snow aggregates, graupel, and hail. In the HUCM SBM scheme [*Khain et al.* 2011], *i* represents liquid droplets, three types of ice-crystal shapes (column, dendrite, and plate), snow aggregates, graupel, or hail. The PSD in bulk cloud microphysics schemes is typically assumed to be a three-parameter gamma distribution:

$$N(D) = N_0 D^{-\mu} exp(-\Lambda D) \qquad \text{Eq. 2}$$

where N_0 is the intercept parameter, μ is the shape parameter, and Λ is the slope parameter. In contrast, the HUCM SBM scheme explicitly predicts *N(D)* through discretization over 33 or 43 particle size bins.

The size-integrated Mueller scattering matrix is further integrated for all species.

$$S|_{tot} = \sum_i S|_i \qquad \text{Eq. 3}$$

where $S|_{tot}$ (mm^2 m^{-3}) represents a total CRM-grid-volume Mueller scattering matrix wherein particle number concentrations and species consistent with the microphysics scheme are integrated. Finally, volume polarimetric radar observables (Z_h, Z_{dr}, K_{dp}, ρ_{hv}) are derived from the integrated scattering matrix, $S|_{tot}$.

Horizontally polarized reflectivity (Z_h, mm^6 m^{-3}, dBZ= 10*log(Z_h)) is expressed as

$$Z_h = \frac{4\pi\lambda^4}{|k|^2\pi^5}\left(\frac{S_{11}|_{tot} - S_{12}|_{tot} - S_{21}|_{tot} + S_{22}|_{tot}}{2}\right) \qquad \text{Eq. 4}$$

where λ is the radar wavelength (mm) and $|k|^2$ is the dielectric factor of water.

Differential reflectivity (Z_{dr}, unitless) is the ratio between the horizontal (H) and vertical (V) polarized reflectivities, generally expressed in logarithmic scale:

$$Z_{dr} = 10\, log_{10}\left(\frac{Z_h}{Z_v}\right) \qquad \text{Eq. 5}$$

where Z_v (mm^6 m^{-3}) is defined as

$$Z_v = \frac{4\pi\lambda^4}{|k|^2\pi^5}\left(\frac{S_{11}|_{tot}+S_{12}|_{tot}+S_{21}|_{tot}+S_{22}|_{tot}}{2}\right) \qquad \text{Eq. 6}$$

Z_{dr} (dB) is a measure of the size-weighted mean oblateness of particles in the Rayleigh scattering regime (i.e., weather radar) and is also sensitive to particle phase (liquid vs. ice).

The co-polar correlation coefficient (ρ_{hv}, unitless) between the H- and V-polarization waves [*Jameson* 1989] can be used to assess the diversity in particle shapes and phases in a pulse volume and is given by:

$$\rho_{hv} = \left(\frac{\sqrt{(S_{33}|_{tot}+S_{44}|_{tot})^2+(S_{43}|_{tot}-S_{34}|_{tot})^2}}{\sqrt{Z_h Z_v}}\right) \qquad \text{Eq. 7}$$

In order to calculate the specific differential phase (K_{dp}, ° km^{-1}), the 4×4 size-species-integrated extinction matrix ($\boldsymbol{K}|_{tot}$, m^2 m^{-3}) is needed. This is derived from the forward component of the size-species-integrated 2×2 scattering amplitude matrix ($f^{(0)}\big|_{tot}$, m m^{-3}).

$$K_{4,3}\big|_{tot} = Im(M_{hh} - M_{vv}) \qquad \text{Eq. 8}$$

where

$$M_{hh} = \frac{\lambda}{1000}\, f_{hh}^{(0)}\Big|_{tot} \qquad \text{Eq. 9}$$

$$M_{vv} = \frac{\lambda}{1000}\, f_{vv}^{(0)}\Big|_{tot} \qquad \text{Eq. 10}$$

where λ is radar wavelength (mm) and 1000 is the unit conversion from mm to m. Specific differential phase is then defined as [*Sachidananda and Zrnic* 1986]:

$$K_{dp} = \frac{180}{\pi} K_{4,3}\big|_{tot} \cdot 1000 \qquad \text{Eq. 11}$$

where the units of K_{dp} are given in deg km^{-1}, 1000 is the unit conversion from m to km. K_{dp} is sensitive to the axis ratio and total mass content.

Actual integration of T-matrix and Mueller matrix modules over size distributions and species, and grids are very time consuming task. Straightforward calculation of radar observables from the regular WRF grid cost several hours with a few thousands of processors. Thus, we have developed efficient look-up table (LUT) approach. With assumptions of particle axis ratio and orientation angle distributions, 4×4 Mueller scattering matrix and 2×2 forward scattering amplitude matrix are calculated for ranges of size bin, temperature, and radar elevation angle for a specific radar frequency and a specific microphysics scheme. This LUT generation process can be scaled up to a few thousands processors, which can generate one LUT within a few minutes. Therefore, the framework allows us test different assumptions of particle shape and orientatino angle distributions (Section 3).

2.1.2 Radial Velocity

Radial velocity (V_{rad}) is computed using the particle terminal velocity at reference pressure level, wind, pressure, and radar scanning geometry. Doppler velocity from a single particle species is calculated from integrating the backscatter-weighted terminal velocity over the particle sizes:

$$V_{dop}|_i = \frac{\int V_t\,(D)|_i\ \beta(D)|_i dD}{\beta|_i} \qquad \text{Eq. 12}$$

, where $\beta|_i$ is the size-integrated backscattering coefficient.

$$\beta|_i = \int \beta(D)|_i dD, \qquad \text{Eq. 13}$$

$$\beta(D)|_i = S_{11}|_i - S_{12}|_i - S_{21}|_i + S_{22}|_i \qquad \text{Eq. 14}$$

The final velocity is obtained by further integrating over the Doppler velocity of all species, adjusting the pressure from the reference state, and then subtracting vertical wind velocity (w).

$$V_{dop}|_{tot} = \sqrt{\frac{P_r}{P}}\ \frac{\sum_i V_{dop}|_i\ \beta|_i}{\sum_i \beta|_i} - w \qquad \text{Eq. 15}$$

The direction of $V_{dop}|_{tot}$ is normal to the ground (along the vertical direction of the CRM). The radial velocity is represented by

$$V_{rad} = -\left[u\cos(\alpha_u) + v\cos(\alpha_v) + V_{dop}|_{tot}\ cos(\cos(\alpha_w))\right] \qquad \text{Eq. 16}$$

where α_u, α_v, and α_w are the angles between the grid-instrument vector, and u and v are the eastward and northward wind components, respectively. The negative sign is defined here as a radial velocity toward the radar.

2.2 iPOLARRIS: Retrieval, Diagnostics, and Visualization

One of the most difficult aspects of comparing models and radar observations is the interpretation of polarimetric radar signals. To address this, the radar community applies retrieval algorithms which convert radar observations into single, more relatable quantities, such as HID. To utilize this in comparison with CRMs, an inverse framework, termed iPOLARRIS, has been developed to apply the same retrieval algorithms and analysis tools to different types of gridded datasets. iPOLARRIS is a set of retrieval algorithms that can be executed on either simulated model data through POLARRIS-f output or on polarimetric and dual-Doppler radar observations in a visually and algorithmically consistent manner. This streamlined framework allows for the mutual benefit of validating radar retrieval algorithms and /or model microphysics and dynamics. For example, the assumptions made in the HID can be tested for consistency with model fields (i.e., the mixing ratios of various species) while the simulated polarimetric HID can be analyzed against observations to diagnose/ evaluate different model microphysical schemes. The iPOLARRIS framework allows for streamlined statistical analysis of model data and observations, such as contoured frequency with altitude diagrams (CFADs, Yuter and Houze [1995]), echo top heights, and vertical velocity characteristics. iPOLARRIS is Python-based and incorporates a library of radar processing algorithms available through the CSU Radar Meteorology group (such as HID, polarimetric rainfall estimation, liquid and ice water path calculations, and up/ downdraft statistics; https://doi.org/10.5281/zenodo.1035908). Example retrievals are described in the following sections.

2.2.1 HID

HID has become a valuable tool for analyzing bulk microphysics from polarimetric radar. HID has been applied to several precipitation radar wavelengths from S- to X-band [*Vivekanandan et al.* 1999; *Straka et al.* 2000; *Keenan* 2003; *Park et. al* 2009; *Dolan and Rutledge* 2009; *Snyder et al.* 2010; *Dolan et al.* 2013; *Bechini and Chandrasekar et al.* 2015]. Many of these algorithms apply fuzzy logic techniques requiring membership functions to calculate a score for different meteorological categories based on the input observations. Although some algorithms have attempted to achieve classification methods based on the data itself [*Wen et al.* 2015], typically the membership functions (MBFs) are based on objectively and subjectively determined ranges of polarimetric variables. However, it is notoriously difficult to validate any hydrometeor classification due to the lack of robust *in situ* observations. By running HID on model-derived data, the HID algorithm itself can be evaluated in a self-consistent manner, as long as cloud simulations and forward operators are robust enough for microphysical consistency.

The fuzzy logic HID described in *Dolan and Rutledge* [2009] and *Dolan et al.* [2013] has been implemented in iPOLARRIS and is used herein to demonstrate the sort of analysis POLARRIS can facilitate. The algorithm requires temperature, polarimetric data, and radar wavelength and then determines the bulk hydrometeor type at a given point using theoretically-based MBFs. For model data, the environmental air temperature at every grid point is used, while for observations, the closest atmospheric sounding in space and time is used and interpolated to the radar analysis grid. Ten categories are allowed in the HID: drizzle (DZ), rain (RN), ice crystals (IC), dry snow (DS), wet snow (WS), vertical ice (VI), low-density graupel (LDG), high-density graupel (HDG), hail (HA), and "big" drops (BD). Vertical ice is a special case where anisotropic ice crystals are aligned in the vertical due to the presence of an electric field, which is not readily simulated in the current CRM configuration. Thus, the CR and VI categories are grouped together in the CR field.

2.2.2 Vertical Velocity

Comparison of kinematic fields from observations and models is challenging. Radar retrievals of the horizontal wind generally rely on vector decomposition of two independent radial velocity measurements (i.e., so-called dual- or multi-Doppler analysis); the vertical velocity then is derived through integration of the anelastic mass-continuity equation [e.g., *Mohr and Miller* 1983; *Potvin et al.* 2009]. More accurate winds can be recovered if particle fall velocity is accounted for in the vertical wind component. Presently, reflectivity-fall velocity relationships for snow, ice, and rain with Giangrande et al. [2013] reflectivity-fall speed (Z_h-V_t) relationships are used to remove the component of the observed radial velocity due to hydrometeor fall speed. The Z_h-V_t relationship is selected based on HID classifications, where low- and high-density graupel and hail are grouped into 'ice' and ice crystals, aggregates, and vertical ice are considered 'snow'. A fall speed is not retrieved for HID classifications of wet snow (e.g. melting layer). Such radar retrievals can then be compared to *u*, *v*, and *w* winds from model fields. An added functionality in iPOLARRIS is to again test the retrieval algorithms by applying the radar dual-Doppler algorithm from two POLARRIS-f simulated radial velocity fields and comparing with the model *u*, *v*, and *w* fields as well as the observation-derived 3D wind field. This capability will be shown in a future study.

2.3 WRF simulations

To demonstrate the utility of POLARRIS, the Advanced Research Weather Research and Forecasting model (WRF-ARW; http://www.wrf-model.org/index.php) is used to simulate a continental mesoscale convective system (MCS) over the Southern Great Plains (SGP) during the Midlatitude Continental Convective Clouds Experiment (MC3E) field campaign [*Jensen et al.* 2016]. WRF was configured with a triple-nested domain (with 9 km, 3 km, and 1 km horizontal-grid spacing) and driven by NCEP Final

Operational Global Analysis (FNL). Simulations using different reanalysis data were also conducted, with results showing differences in location and timing of convection, but microphysical statistics varied little when sampled separately for convection and stratiform regimes (not shown). The location and the number of grid points of the finest domain are similar to those in previous works [*Iguchi et al.* 2012a; *Tao et al.* 2013]. The WRF simulations were initialized at 1200 Z on 23 May 2011 and integrated for 24 hours. Output was generated at 10-minute intervals.

This study utilizes two microphysical packages: the Goddard single-moment 4ICE microphysics [*Lang et al.* 2014; *Tao et al.* 2016] and HUCM SBM [*Khain et al.* 2000, 2011; *Phillips et al.* 2007; *Iguchi et al.* 2012b,c]. The Goddard 4ICE and HUCM are well suited for simulating intense midlatitude convective systems owing to the explicit hail category [*Iguchi et al.* 2012c, *Tao et al.* 2016], but the two schemes are very different in degree of complexity and therefore provide a good demonstration of POLARRIS capabilities. The intent herein is not to compare and improve these specific schemes.

The single-moment 4ICE essentially predicts the mass mixing ratio of bulk microphysics species (cloud, rain, ice, snow aggregates, graupel, and hail) and is a significant improvement over the previous 3ICE scheme [*Lang et al.* 2014]. Improvements include a number of new ice process functionalities as well as PSD mapping schemes adjusted with respect to ground-based radar measurements. A mass-dimension relationship (i.e., effective density) for snow aggregates is based on *in-situ* 2D video disdrometer (2DVD) data from along the Front Range of eastern Colorado

[*Brandes et al.* 2007]. All of the PSD and density information are consistent with POLARRIS-f.

HUCM SBM is based on a scheme from the Hebrew University Cloud Model [*Khain et al.* 2011] and has been tested for a cold-season snowstorm case [*Iguchi et al.* 2012a], an MC3E midlatitude case (*Iguchi et al.* 2012b), and high-latitude mixed-phase precipitation events [*Iguchi et al.* 2014]. The PSD of each hydrometeor category is explicitly calculated over 43 mass bins spanning particle mass sizes from 3.35×10^{-11} g to 1.47×10^{2} g (ranging from nucleation particles up to cm-scale hail stones). Additionally, bin-by-bin melt fractions are also calculated for the snow aggregate, graupel, and hail categories [*Phillips et al.* 2007; *Iguchi et al.* 2014]. Snow aggregates account for explicit calculation of bin-by-bin riming of supercooled water allowing for smooth transitions of bulk effective density from fluffy snow aggregates to dense graupel/hail particles, omitting any spontaneous snow-to-graupel/hail autoconversion processes between these categories. Both HUCM SBM and 4ICE use a power-law mass-dimension relationship. 4ICE snow aggregates have a higher density than the HUCM SBM as the 2DVD included some degree of riming at ground level [*Brandes et al.* 2007]. HUCM snow aggregate density is for pure dry aggregates and much lower without riming (not shown), but explicit riming can still increase the density toward graupel [*Iguchi et al.* 2012b]. All of these physical parameters are consistently represented in POLARRIS-f.

However, the SBM used in this study does not yet include time-dependent rain freezing or wet growth of hail/graupel [*Phillips et al.* 2014, 2015], which limits the understanding of polarimetric signals of partially-melted hail/graupel in the mixed-phase zone. As bright band evaluation [e.g., *Iguchi et al.* 2014] is not in the scope of this study, mixed-phase particles (air-ice-liquid mixture) are not considered in POLARRIS-f. The main focus of this study is on the uncertainties related to the ice species particularly related to the axis ratio and orientation angle assumptions.

3 Assumptions and Uncertainties in POLARRIS

While size distributions, effective density, and phase are assumed or predicted by either bulk or bin microphysics schemes, particle axis ratio and/or orientation angle distributions are not considered in most microphysics schemes. Thus, a critical component of POLARRIS-f is determining appropriate values of these parameters in order to precisely reproduce polarimetric radar variables (e.g., Z_{dr}, K_{dp}). Axis ratios (aspect ratio, *A*) of rain drops have been extensively investigated, yielding various empirical relationships representing the oblateness of raindrops as a function of diameter [e.g., summarized in *Beard and Chuang* 1987]. *Matrosov et al.* [1996] investigated axis ratios for different ice crystal habits in a limited case. However, very few studies have reported on axis ratio distributions for precipitating solid particles such as snow aggregates, graupel, and hail, which are difficult to measure and may depend upon the environment and storm type. Thus, the impact of these uncertainties on POLARRIS-f results are investigated in this study.

Figure 1 shows the scattering geometry of an oblate particle with a specific particle symmetry axis ($\vec{N}$) in the cartesian coordinate (X, Y, and Z axis) [e.g., *Holt* 1984; *Vivekanandan et al.* 1991]. Particle orientation angle is represented by two parameters (θ and ϕ). In general, ϕ is assumed to be randomly oriented so there is no preferred orientation angle in the X-Y plane; however, most previous studies did measure some preferred orientation angles with respect to the vertical axis (θ). Therefore, hereafter, "particle orientation angle" refers to θ (the angle between the particle symmetry axis and the vertical axis) in this manuscript.

Most previous studies [e.g., *Jung et al.* 2010; *Ryzhkov et al.* 2011; *Putnam et al.* 2017; *Kollias and Tatarevic* 2017] assumed a Gaussian angle distribution, where the mean orientation angle ($\bar{\theta}$) and standard deviation (degree of particle tumbling σ) are used to describe particle orientation behavior via

$$\Delta(\theta) = \frac{1}{\sqrt{2\pi}\sigma} exp\left[-\left(\frac{\theta-\bar{\theta}}{\sqrt{2}\sigma}\right)^2\right] \qquad \text{Eq. 17}$$

A limited study of the orientation behavior of planar crystals also confirmed the Gaussian distribution in orientation angle [*Sassen* 1980]. Fall behaviors of other ice particles are less known, particularly snow aggregates, graupel, and hail [section 10.5.3, *Pruppacher and Klett* 1997; *Straka et al.* 2000].

Table 1 shows three sets of assumptions tested herein derived from recent studies as well as this study. *Ryzhkov et al.* [2011] (RY11) and *Kollias and Tatarevic* [2017] (CR-SIM) use nearly identical assumptions so RY11 is used to represent both. Similarities and differences between RY11, Putnam et al. [2017] (referred to as PU17) assumes more oblate particles with smaller standard deviation (σ) than RY11, and this study (denoted as MA18) proposes a few non-traditional assumptions for comparison purpose. Note that this paper does not intend to conclude whether a specific assumption is more accurate or not due to limitation from available observations. All cloud species are assumed to be spherical. For bulk microphysics, randomly oriented ice columns are assumed for simplicity; therefore ice crystal particle does not contribute to Z_{dr} and K_{dp} values. SBM includes plates and dendrites, which can contribute to Z_{dr} and K_{dp} values

(Table 1). The distributions of rain axis ratio and orientation angle are unified following *Brandes et al.* [2011]. Thus, differences in Z_{dr} and K_{dp} between RY11, PU17, and MA18 is due to the different assumptions in snow aggregate, graupel, and hail in this study (Table 1).

In this study, snow aggregate axis ratio model is derived from the MC3E field campaign using particle probes outfitted on the UND Citation II aircraft. We have collected nine three-minute samples of snow aggregate images from the HVP-3 probe (Dr. A. Bansemer, personal communication), and estimated axis ratio following *Korolev and Isaac* [2003]. Axis ratio is furthered binned as a function of particle diameter to estimate the following empirical relationship for diameter (D) less than 10 mm, while it is constant value of 0.5 for diameter greater than 10 mm.

$$A_{xis} = 0.7 - 0.05D + 0.003D^2 \; (D < 10 \text{ mm}) \qquad \text{Eq. 18}$$

Hendry et al. [1987] examined radar observations using circular polarization, and estimated standard deviation of snow orientation angle from 15° to 30° within moderate-to-heavy snow. This study assumes mean orientation angle and standard deviation identical to PU17 ($\bar{\theta} = 0°$, σ=20°).

Graupel axis ratio and orientation angle distributions are rarely reported [*Straka et al.* 2000]. We have used the statistical distributions of aspect ratio and orientation distributions of graupel from a Multi-Angle Snowflake Camera (MASC) at Utah Mountain [*Garrett et al.* 2015]. Despite the sampling points being limited to a single location and time of year, this is one of the only sources of observations using modern instruments. MASC utilizes three cameras to characterize three-dimensional shapes of falling snow aggregate and graupel. Based on interpretation of the normalized histogram derived in *Garrett et al.* [2015] via Eqn. 17, we treat a peak of absolute orientation angle distribution as the mean axis ratio ($\bar{\theta}$ = 20°), and calculated the standard deviation of 42° and mean axis ratio (A_{xis} =0.814) for graupel. This non-traditional assumption is quite different from RY11 and PU17, especially the non-zero mean orientation angle. However, large standard deviation tends to smear out polarization signals (see the section 4.2).

The assumed hail axis ratio in this study is estimated from the observations recorded in *Knight* [1986]. Samples from three locations (Oklahoma, N.E. Colorado and Alberta) of hail axis ratios are averaged for each sampled size bin and weighted by sampling number to derive the following 2nd-order polynomial fit:

$$A = \max(0.725, 0.897 - 0.0008D - 0.0002D^2) \qquad \text{Eq. 18}$$

The orientation angle and fall behavior of hail is also uncertain. *Straka et al.* [2000] summarized observational and modeling studies showing typical Z_{dr} values of hail in the range -2 dB 0.5 dB for sizes from 20 to 40 mm at S-band frequency. *Aydin et al.* [1986] showed the Z_H-Z_{dr} scatter plots from S-band polarimetric radar, indicating the negative Z_{DR} for very large Z_H (~ 60 dBZ). Theoretical calculation from *Depue et al.* [2007] and *Ryzhkov et al.* [2013] suggest that the negative Z_{DR} is due to the strong resonance scattering due to melting oblate hail with its maximal dimension in the horizontal. For contrasting reasons, this study assumes the mean orientation angle $\bar{\theta}$ = 90° is adopted to one of the assumption examined in *Vivekanandan et al.* [1991], while we assume large standard deviation (40°) similar to the RY11. This assumption has a slightly different impact on radar observables than assuming prolate hail with $\bar{\theta}$ = 0º in that it does not produce as much of a resonance scattering effect. Such an effect will be pronounced in the simulated Z_{dr} statistics. All the different assumptions (Table 1) are tested in the next section.

4 Results and Discussion

Radar data for this study are derived from the U. S. Department of Energy (DOE) C-band scanning precipitation radar (CSAPR). The data were quality controlled, bias- and attenuation corrected using the specific differential phase with a big drop correction [*Carey et al*. 2000], and K_{dp} was calculated using the *Wang and Chandrasekar* [2008] methodology. Some regions of extreme differential attenuation (-6 dB) from large voluminous rain core were noted during this case, which were too significant for the applied correction methodology. Thus Z_{dr} values below -1 dB have been removed from the analysis hereafter. Note that these strong negative Z_{dr} signals are not associated with oblate melting hail [*Ryzhkov et al.* 2013], since they are not associated with strong reflectivity (i.e. convective cores). Three dimensional winds were derived from the DOE SGP radar network including CSAPR, two X-band scanning radars (XSAPRS), and the nearby NEXRAD KVNX WSR-88D radar by applying the multi-Doppler CEDRIC mass-continuity methodology [*Mohr and Miller* 1983].

The forward model (POLARRIS-f) assumes observation-consistent C-band radar frequency and radar coverage (118 km maximum radar range) to calculate polarimetric radar observables and radial velocity. The radar instrument geolocation is also consistent to the CSAPR (36.796°N and 97.451°W) in the WRF-SBM simulations; however, due to a southward shift of convection in the simulations, the radar instrument is adjusted 0.5° southward in the WRF-4ICE simulation. Figure 2 shows the evolution of radar reflectivity at 2 km AGL at three times from the CSAPR and WRF-SBM and WRF-4ICE simulations. Convective echoes are present within the CSAPR domain from 22 Z May 23 to 00 Z May 24. The WRF-SBM run has strong convection within the radar sampling area; the WRF-4ICE run has less convective coverage at 22 Z than the SBM, but its reflectivity structure is more realistic at 00 Z May 24. Although the exact spatial structures are not captured by the WRF simulations, both reproduce the range of reflectivities in both the convective (up to 64 dBZ) and stratiform precipitation.

4.1. Cross-Sections of Polarimetric Radar Observables and Retrievals

Figure 3 shows horizontal cross-section images at a height of 2 km above mean-sea level (MSL) of the CSAPR radar observations (Z, Z_{dr}, K_{dp}, ρ_{hv}, and V_{rad}) and retrievals (wind vectors and HID) at 2148 Z on May 23. Convective cells within the radar domain reach 60 dBZ with high Z_{dr} (>3.0 dB) and K_{dp} (2.5 ° km^{-1}), all of which suggest the presence of large oblate raindrops and appreciable water contents. These are mostly categorized as rain (RN) or big drops (BD) in the HID; the thick red contours in Fig. 3a mark the convective cores using the separation method in *Powel et al* [2016]. The stratiform regions are generally categorized as drizzle (DZ) with relatively low reflectivity (< 35 dBZ) and smaller Z_{dr} (< 1.0 dB) and K_{dp} (< 0.5 ° km^{-1}) values. Radial velocity (V_r) and wind vectors indicate strong convergence in the most intensive convective cores in the southwest portion of the radar domain (Fig. 3f).

Figure 4 shows horizontal cross-section images of C-band radar parameters from the WRF simulation with HUCM SBM at 00 Z on 24 May. Note that the 00 Z field is used to best match the morphology of the observations presented in Fig. 2. The radar observables are simulated from POLARRIS-f using the MA18 axis ratio and orientation angle distribution assumptions. Identical convective-stratiform separation [*Powel et al.* 2016] and HID retrievals [*Dolan et al.* 2013] are derived using iPOLARRIS. The strong convective core and associated horizontal wind convergence is captured in the middle of the radar domain, where the radar reflectivity reaches greater than 60 dBZ with very high Z_{dr} (> 2 dB) and K_{dp} (> 2.5 ° km^{-1}). Similar to the observations, these simulation results suggest the presence of large raindrops and appreciable water contents.

Figure 5 shows horizontal cross-section images from the WRF simulation using the 4ICE bulk microphysics at 00 Z on May 24, again for C-band and with MA18 assumptions. The radar reflectivity in the convective core reaches ~55 dBZ, and Z_{dr} and K_{dp} ranges up to 3.0 dB and 2.5 ° km^{-1}, respectively. Similar to the WRF-SBM simulation, the WRF-4ICE simulation produces reasonable ranges of polarimetric radar signals in the convective cores (discussed more quantitatively later). Both WRF-SBM and WRF-4ICE capture the depressed ρ_{hv} values within the convective core apparent in the CSAPR data. However, WRF-4ICE has a much wider region of ρ_{hv} below 0.97 (Fig. 5e), while WRF-SBM has a very limited area with ρ_{hv} below 0.96 (Fig. 4e).

Figure 6 shows observed vertical cross-sections of radar observations along east-west transect 10 km north of CSAPR at 2148 Z on May 23. CSAPR shows that a strong convective core is present ~40 km east of the radar domain with echoes greater than 50 dBZ reaching to 13 km MSL (Fig. 6b). K_{dp} values within the raining region of the convective core are around 2.5 ° km^{-1} (Fig. 6d), while Z_{dr} reaches 3.0 dB (Fig. 6c). The HID indicates the presence of hail (HA) and big drops (BD) surrounded by low- and high-density graupel (LDG and HDG) (Fig. 6a). The width of this convective core exceeds 10 km and the vertical velocity peaks at 20 m s^{-1} (Fig. 6f). On the other hand, the stratiform region is dominated by snow-aggregates (AG) (Fig. 6a). The presence of the melting layer is denoted by the wet snow (WS) category. Stratiform reflectivity signatures remain below 35 dBZ, and Z_{dr} ranges from 0 to 1 dB with near-zero K_{dp}, suggesting the presence of low-density, nearly spherical snow aggregates. Reflectivities near the surface are weak to moderate up to 30 dBZ, and there is no significant positive Z_{dr} and K_{dp}, suggesting the presence of small raindrops/drizzle.

Similar vertical cross-sections of WRF-SBM (4ICE)-simulated radar observables and HID are shown in Fig. 7 (Fig. 8). Corresponding distributions of SBM-simulated hydrometeor mass concentrations (g m^{-3}) are also shown for comparision to the HID algorithm. These mass concentrations include ice (qi: sum of dendrites, needles, and plates), cloud (qc: liquid class < 100 μm radius), rain (qr: liquid class > 100 um radius), snow (qs: aggregates with explicit riming fraction), graupel (qg: graupel), and hail (qh: hail). Around 97.5°E, a very strong convective core reaches up to 15 km MSL with radar echoes up to 60 dBZ (Fig. 7b) and an associated updraft with peak speeds of 25 m s^{-1} (Fig. 7f). The HID profiles show the dominance of hail (HA) and graupel (LDG) in and around the core (Fig. 7a). Vertical profiles of the HID classes are well matched with the corresponding SBM mass concentrations in convective cores as well as stratiform regimes. For example, in the stratiform region, HID indicates the presence of ice crystals, aggregates, low-density graupel, and drizzle from the cloud top toward the surface similar to the SBM mass concentration transitions.

While variability of the reflectivity and the vertical velocity are similar in magnitude to the observations (Fig. 6), the simulated Z_{dr} and ρ_{hv} appears to be much more homogeneous in the ice regions compared to observations (Fig. 7c and 7e). Notably, the observed ρ_{hv} ranges from 0.95 to 0.98 (Fig. 6e), while the simulated ranges from 0.99 to 1 (background is 1.) (Fig. 7e). Depression of the background ρ_{hv} in the observations could be related to systematic factors, which are not modeled by the T-matrix/ Mueller matrix, e.g., receiver noise in each channel, antenna mis-match, cross-coupling, non-uniform beam filling, beam broadening, etc. [*Zrnic et al.* 2006; *Ryzhkov* 2007]. The lack of high density graupel in favor of low-density graupel in the SBM HID compared to observations is noted.

In comparison with the SBM, 4ICE (Fig. 8) produces narrower convective cores characterized with hail (HA) and low-density graupel (LDG), which is actually more closely aligned to the observations (Fig. 6). In the surrounding stratiform area, ice crystals (CR) generally dominate the HID profile above the 0°C isotherm (Fig. 8a). Snow aggregates (AG) are sporadically present closer to the 0°C isotherm level (HID), although snow mass concentrations (Fig. 8o) from direct model output indicate a large amount of snow aggregates present in the simulation. These issues are further investigated in Sec. 4.2.

4.2. Sensitivity of the Polarimetric Radar Observables to Particle Assumptions

In this section, the polarimetric observables and retrievals are compared statistically in the form of CFADs using the three different assumptions on particle orientation angle distributions and axis ratio in Table 1. The radar observables are computed at C-band radar frequency (6.25 GHz) to be consistent with the CSAPR observations. The analysis is performed during the most intense time period from 2300 Z on May 23 to 0130 Z on May 24 using 10 min intervals for model output. The CFAD color-scale is set to highlight the most frequent occurrences (colored), while gray scales represent considerably lower frequencies (below 0.5%).

Figure 9 shows CFADs of Z_{dr} and K_{dp} from the convective and stratiform region of the CSAPR observations compared to the WRF-SBM run using the three sets of assumptions for particle shapes and orientation angles (Table 1). The observed convective Z_{dr} distribution shows a wide range of frequencies (defined as > 0.05 % in the color shades) ranging from -1 to 0.5 dB around 14 km MSL, where high frequencies of negative values could indicate the presence of vertically aligned anisotropic ice crystals in a strong electric field or attenuation correction issue associated with very strong rain core. Z_{dr} in the 5-10 km MSL height range exhibits a narrower distribution from -0.5 to 0.9 dB, whereas at heights below the 0°C isotherm, the distributions have much larger values with higher variability (from 0.5 to 5.5 dB), the largest values associated with large oblate raindrops. The observed stratiform Z_{dr} shows similar distributions to the convective one, except Z_{dr} below 2km MSL is narrowly distributed (up to 2 dB).

The WRF-SBM simulated convective and stratiform Z_{dr} values are more narrowly distributed especially for the MA18 and RY11 assumptions than those of the observations. PU17 has slightly wider distributions (from 0.0 to 1.0 dB, mode centered at 0.8 dB) than the MA18 and RY11 above the 0°C isotherm level, but they have a positive bias. In rain, all three assumptions use the identical parameterization from *Brandes et al*. [2011], leading to values from 1.5 to 2.5 dB in the convective region and 0 to 1.5 dB in the stratiform; whereas the observations extend to 5 dB. Despite a very low frequency (< 0.05%), wide ranges of negative Z_{dr} are present in the PU17 and RY11 assumptions due to the resonance effect of Mie scattering from large horizontally-oriented oblate hail particles, while the vertically-oriented oblate hail assumption in MA18 do not have a resonance effect. Thus, hail assumptions in PU17 and RY11 could be more realistic.

The observed convective K_{dp} has a narrow distribution in the solid-precipitation zones, centered at 0 ° km^{-1} with a slight negative excursion between 10 and 12 km MSL. In the rain zone, distributions of K_{dp} are wide with the most frequent values between -0.6 and 2.0 ° km^{-1}. The observed stratiform K_{dp} has even narrower distributions. All assumptions exhibit too wide distributions of K_{dp} especially between 8 and 15km MSL due to presence of horizontally oriented plate ice crystals. With PU17, more oblate particle shapes and smaller standard deviations of orientation angle for small frozen hydrometeors result in broader CFADs, especially in K_{dp}. Despite the different assumptions of axis ratio and orientation angle distributions in snow, graupel, and hail, Z_{dr} and K_{dp} distributions appear to be similar between MA18 and RY11.

Figure 10 shows CFADs from the WRF-4ICE simulations using the three particle assumptions. The WRF-4ICE Z_{dr} CFADs are more variable among the three assumptions than with the SBM and have differing structures compared to WRF-SBM. The MA18 Z_{dr} values between 8km and 16km MSL are bi-modally distributed. The near-zero Z_{dr} values are due to the 90-degree oriented oblate hail assumptions, while the positive Z_{dr} peak is due to the near-horizontally oriented oblate snow aggregates; this 2nd mode does not appear in the WRF-SBM Z_{dr} values. The PU17 Z_{dr} values are mostly centered around 1.0 to 1.2 due to horizontally oriented oblate snow, graupel, and hail, while the RY11 has the narrowest and the smallest Z_{dr} values in the ice region, again due to having large tumbling assumptions. The MA18 and PU17 assumptions result in unrealistically large

K_{dp} values for both convective and stratiform regions above the 0°C isotherm level; RY11 produces the most realistic, narrow distributions of K_{dp} for WRF-4ICE case.

Figures 9 and 10 provide an overall depiction of the polarimetric radar observables from the observations and the simulations for both SBM and the 4ICE microphysics using different assumptions for axis ratio and orientation angles for both the convective and stratiform precipitation regimes. No single set of assumptions accurately reproduced the observed Z_{dr} and K_{dp} distributions in either the convective or stratiform regions. Interestingly, these assumptions affect the Z_{dr} and K_{dp} distributions differently for the bin and bulk schemes. For example, MA18 produces broader Z_{dr} and K_{dp} distributions than the RY11 in the 4ICE scheme but the reverse in the SBM, pointing to possible critical differences between the explicit and bulk approaches in terms of their PSDs.

To this end, detailed PSDs of solid particles are compared between the simulations and available aircraft observations from the Citation II for this case. Figure 11 shows the PSD (solid black) measured from the Citation HVPS-3 on May 23 at a height of around 8 km. In comparing the aircraft flight track, particle images from the high-resolution cloud particle imager (CPI), and CSAPR-derived HID (not shown), it was found that the sampled particles mostly represent snow aggregates in the stratiform region. Blue solid and dotted lines represent PSD assumptions for the aggregate category in *Dolan and Rutledge* [2009] and *Dolan et al.* [2013] (the same algorithm used in this study for HID). Corresponding PSDs are derived from the WRF-SBM and WRF-4ICE simulations similar to the aircraft estimation method [*Iguchi et al.* 2012b]. It essentially re-samples the model bulk or bin microphysics PSD into the aircraft-measurable bulk

PSD bins and integrates over the particle maximum diameter and the domain to estimate the mean PSD. In this study, simulated ice crystals and aggregate species between 7 km and 9 km of altitude are sampled to construct the aircraft-measurable bulk PSD, consistent to the actual measurement patterns of the Citation aircraft.

In MC3E, similar to the Citation aircraft observations during the MC3E (not shown here), PSDs in Fig. 11 are dominated by snow aggregates. The sampling period is identical to that for the CFADs, from 2300 Z on May 23 to 0130 Z on May 24 using model output every 10 minutes. 4ICE (green solid) has a much steeper curve, close to the assumption of DR09 assuming an equivalent snowfall rate of 0.5 mm hr^{-1}. SBM (red solid) has a similar PSD to the 4ICE and DR09 (0.5 mm hr^{-1}) until the 4 mm diameter bin but is bi-modally distributed with the secondary mode around 8 mm in diameter. Therefore, part of the explanation for the smaller Z_h and larger K_{dp} distributions compared to observations is related to this narrow snow aggregate PSD in 4ICE. Resultantly, the low Z_h and relatively high K_{dp} lead the HID algorithm to classify model snow aggregates as "ice crystals" (Fig. 8a).

4.3 Statistics of HID Retrievals

In this section, a probability-based analysis of the polarimetric radar retrievals of HID is discussed. As noted earlier, all polarimetric parameters (Z, Z_{dr}, K_{dp}, and ρ_{hv}) from observations and POLARRIS-f calculations from WRF SBM/4ICE simulations output the same exact radar retrievals within iPOLARRIS. Thus, radar retrievals are derived in a consistent manner between the observations and simulations. *Putnam et al.* [2017]

conducted a very similar approach and compared the HID between observations and simulations with a number of different bulk microphysical schemes in 0.5°-tilt images. To carry out a more comprehensive analysis, we have constructed “stacked frequency by altitude diagrams” (SFADs) of the HID integrated over intense precipitation periods. The SFADs represent the relative frequency of each identified hydrometeor type at each height.

Figure 12 shows HID SFADs from CSAPR observations. The HID observations from CSAPR show that heavily-rimed particles (HA, LDG and HDG) occupy ~20-50% of the convective region, whereas AG and CR dominate in the stratiform region above the 0°C isotherm level. These vertical fractions of ice hydrometeor are critical for evaluating the CRM simulation ever since the development of bulk microphysics [*Rutledge and Hobbs* 1984].

Figure 13 compares the observed and simulated HID profiles using the three different assumptions for the snow aggregate (AG), graupel (HDG and LDG), and hail (HA) categories. All assumptions applied to both SBM and 4ICE largely underestimate (underestimate) the AG fraction by as much as 40 % in the convective (stratiform) region. Graupel is also largely overestimated by WRF-SBM and WRF-4ICE in both the convective and stratiform regions with overestimations varying appreciably among the different sets of assumptions. For the convective regions, SBM and 4ICE overestimate the hail fraction by up to 35% and 20%, respectively. Uncertainties in the polarimetric radar variables (Z_{dr} and K_{dp}) using the different particle shape and orientation angles affect the HID fraction by up to 20% for the graupel and hail but less so in terms of AG fraction (generally < 10%). Here it can be seen that the particle assumptions all tend toward the same general over- or under-prediction compared to observations, with generally very little spread between assumptions other than the 4ICE convective graupel and SBM stratiform graupel.

Overall, it can be concluded that both WRF simulations tend to over-predict the hail and graupel fractions, while underestimating the proportion of snow aggregates. The different assumptions for axis ratio and orientation angle distributions among MA18, PU17, and RY11 affect the quantitative distributions of Z_{dr} and K_{dp} but do not change this overall conclusion. This implies that despite the uncertainties in the axis ratio and orientation angle, POLARRIS HID can provide a useful model evaluation tool to identify the four-dimensional distributions of bulk hydrometeor class in a qualitative manner.

5 Conclusions

A new framework, POLARRIS, has been developed to compare CRM cloud model simulations with polarimetric radar observations. POLARRIS is comprised of a forward simulator (POLARRIS-f) and an inverse module (iPOLARRIS). POLARRIS-f is based on robust T-matrix and Mueller matrix scattering calculations [*Vivekenandan et al.* 1991] in order to compute polarimetric observables through the consistent assumptions of microphysics size distributions and effective density with effective dielectric constant [*Maxwell Gartnet* 1904; *Bruggeman* 1935; *Debye* 1929; *Bohren and Battan* 1980].

An important aspect of POLARRIS-f is assigning particle axis ratio and orientation angle distributions. These are not typically specified in the majority of microphysics schemes but can have a large influence on the retrieved polarimetric observations. While POLARRIS-f has similar capabilities to other polarimetric radar simulators [e.g., *Ryzhkov et al.* 2011; *Putnam et al.* 2017; *Kollias and Tatarevic* 2017], iPOLARRIS is a unique post-processing component that consistently implements polarimetric radar retrievals and statistical analysis. HID has been used as an example in this study, but iPOLARRIS can be extended to different retrievals, such as precipitation, vertical motion, liquid water contents, and convective-stratiform separation. The model and observations are put into the exact same framework to make consistent comparisons.

Three different sets of assumptions in particle axis ratio and orientation angle distributions from two previous studies [*Ryzhkov et al.* 2011, *Putnam et al.* 2017] alongside a set of assumptions derived for this study were tested for snow aggregate, graupel, and hail particles via WRF simulations of an intense midlatitude convective complex observed during MC3E. The results from any given set of assumptions are qualitatively similar, but quantitatively diverse, particularly in the probability distributions of Z_{dr} and K_{dp}, which are directly related to particle oblateness and orientation angle distributions in addition to the particle density and size distributions.

For hail, the RY11 and PU17 hailstone orientation assumptions appear to be more reasonable than MA18, since the MA18 hailstone assumption does not reproduce resonance scattering signals in Z_{dr}. On the other hand, *Knight and Knight* [1970] showed direct observation of large prolate-shaped hailstone falling along the maximum dimension. Although RY11 and PU17 assumptions agree well with some observational and theoretical calculations [*Depue et al.* 2007; *Ryzhkov et al.* 2013], the natural variability of hail shape and falling behavior could be more complex.

For snow and graupel, none of the assumption sets outperformed the others compared to observed Z_{dr} and K_{dp} CFADs using either SBM or 4ICE microphysics. The simulated Z_{dr} and K_{dp} CFADs are generally either more narrowly or widely distributed in the different cases than the observations. Thus, we conclude that the single model of particle shape and orientation angles are not sufficient assumptions to represent nature of the polarimetric radar observation. These uncertainties were not reported in previous studies [e.g., *Ryzhkov et al.* 2011; *Putnam et al.* 2017; *Kollias and Tatarevic* 2017].

HID seems to be a more stable metric, because the fuzzy-logic methodology synthesizes information from all variables and is heavily weighted by reflectivity. Additionally, the broad membership beta functions encompass a wide variety of assumptions about axis ratio and orientation angle distributions. HID comparisons revealed that all three sets of assumptions applied to both microphysics schemes tended to overpredict hail and graupel in convection, while underestimating the fraction of snow aggregates in this particular case study.

Almost all bulk and bin microphysics schemes do not explicitly predict axis ratio and orientation angle distributions, so that these parameters remain uncertain, in addition to size distributions [*Heymsfield et al.* 2004], effective density [*Heymsfield et al.* 2010], and partially melting particles [*Phillips et al.* 2007]. A few microphysics schemes crudely predict ice crystal and aggregate particle shape [*Hashino and Tripoli* 2011; *Harrington et al.* 2013; *Chen and Tsai* 2016], which can impact not only the ice microphysics processes but also polarimetric observables [*Sulia and Kumjian* 2017]. With the careful analysis of polarimetric radar signals [*Hendry et al.* 1987; *Ryzhkov et al.* 2002; *Ryzhkov, and Zrnic*

2007], these new microphysics schemes will allow us to constrain variability of particle shapes and orientation angle distributions against observations.

Once the simulated microphysics is well evaluated, simulated polarimetric observables along with simulated hydrometeors can be used to examine uncertainties and extend the capability of polarimetric radar retrievals [e.g., *Kumjian and Prat* 2014; *Schrom and Kumjian* 2018] or detailed microphysics process in deep convective cores [*Dawson et al.* 2014]. For such purpose, CRM simulations must resolve radar sampling volumes at eddy permitting scales (Δ=250m) and future simulated radar observables must be re-sampled to be consistent with the radar instrument beam width and range volume. These studies will be presented in future work.

Appendix A. Calculation of Effective Dielectric Constant and Particle Density

The complex dielectric constant (ε) describes the absorption and refraction properties of a medium at a specific wavelength. The dielectric constant for water and ice is largely determined by wavelength and slightly by temperature [*Liebe et al.* 1991; *Hufford* 1991]. Unlike pure liquid drops (cloud and rain), ice particles are often mixed with air and water. These mixtures of dielectric constant can be treated as a single "effective" dielectric constant (ε_{eff}), when each single medium is much smaller than the wavelength, i.e., Rayleigh regime (size parameter: $X=\pi D/\lambda$ ~ 2, where D is particle diameter and λ is wavelength).

Several solutions have been derived through different physical assumptions, including Maxwell-Garnett (MG) [*Maxwell Garnett* 1904], Effective Medium (EM) [*Bruggeman* 1935], and Debye (DB) solutions [*Debye* 1929]. These solutions are compared and evaluated in *Bohren and Battan* [1980]. The MG method assumes a medium of a shell (matrix) and a core (inclusion) so that it always has two solutions between the shell-core (e.g., air-shell and ice core versus ice-shell and air core) assumptions. EM has homogeneous mixing assumptions so that the estimation (ε) falls somewhat between the two MG solutions. DB also assumes a mixed homogeneous medium such as an aqueous medium. *Bohren and Battan* [1980] concluded that particular assumptions appear to be better in particular (mixing) situations so that there is no compelling reason that one scheme is completely superior to the other schemes universally. Here are three formulas for calculating the effective dielectric constant for the three different methods.

MG: $$\epsilon_{MG} = \epsilon_m \left[1 + \frac{3f\left(\frac{\epsilon-\epsilon_m}{\epsilon+2\epsilon_m}\right)}{1-f\left(\frac{\epsilon-\epsilon_m}{\epsilon+2\epsilon_m}\right)}\right] \qquad \text{Eq. A1}$$

EM: $f\left(\frac{\epsilon-\epsilon_{EM}}{\epsilon+2\epsilon_{EM}}\right)+(1-f)\left(\frac{\epsilon_m-\epsilon_{EM}}{\epsilon_m+2\epsilon_{EM}}\right)=0$ Eq. A2

DB: $\frac{\epsilon_{DB}-1}{\epsilon_{DB}+2}=f\left(\frac{\epsilon-1}{\epsilon+2}\right)+(1-f)\left(\frac{\epsilon_m-1}{\epsilon_m+2}\right)$ Eq. A3

In POLARRIS-f, these options are available to calculate air-ice mixture (i.e., for ice crystals, dry snow aggregates, graupel, and hail). Once the effective dielectric constant of an air-ice mixture is derived, it will be further mixed with liquid particles for mixed-phase particles (snow aggregates, graupel and hail) again via the above equations with different physics assumptions. This second process has a much larger impact on simulating the bright band from the thin melting layer so that the choice will be more obvious (not shown here). The effective mixture approximation is inaccurate, when the size parameter (*X*) becomes much larger than ~2 (Mie scattering regime). In this case, a more sophisticated single-scattering model is required. Recently, *Schrom and Kumjian* [2018] compared the polarimetric scattering properties between branched planar crystals and homogeneous oblate particles and found significant errors when calculating the backscattering cross sections of horizontal and vertical polarizations at X-band. Further study is required to better understand the scattering field of complex ice particle in the future.

Acknowledgement

This work is funded by Department of Energy (DOE) Atmospheric System Research (ASR) program (DE-SC0014371). The authors thank the DOE ASR project managers: Drs. Shaima Nasiri and Ashley Williamson, and three anonymous reviewers. We also thank the NASA Advanced Supercomputing (NAS) Division and Center for Climate Simulation (NCCS) (Project Manager T. Lee at NASA HQ) for providing the computational resources to conduct the WRF and POLARRIS simulations. The authors also thank to Dr. A. Bansemer (NCAR) for the aircraft data to construct PSD, T. Garrett (University of Utah) for the MASC data, and Dr. B. Fuchs for assistance with programming *i*POLARRIS. WRF-SBM and WRF-4ICE simulations of the MC3E case are available through NASA GSFC Cloud Library (https://portal.nccs.nasa.gov/cloudlibrary/) upon request. DOE ARM radar data is available from ARM DATA DISCOVERY (http://www.archive.arm.gov/discovery/#v/results/s/fcat::sfcprop). Finally, we thank three anonymous reviewers who significantly improved the manuscript. POLARRIS is available to public (http://radarmet.atmos.colostate.edu/polarris/).

References:

Bechini, R. and V. Chandrasekar, 2015: A Semisupervised Robust Hydrometeor Classification Method for Dual-Polarization Radar Applications. J. Atmos. Oceanic Technol., 32, 22–47, https://doi.org/10.1175/JTECH-D-14-00097.1

Bohren, C. F., and Battan, L. J. (1980), Radar backscattering by inhomogeneous precipitation particles, *J. Atmos. Sci.*, *37*1821-1827. doi: http://dx.doi.org/10.1175/1520-0469(1980)037<1821:RBBIPP>2.0.CO;2

Bruggeman, D. A. G., 1935: Berechnung verschiedener physikalischer Konstanten von heterogenen Substanzen: I. Dielectrizitatskonstanten und Leitfahigkeiten der Mischkorper aus isotropen Substanzen (Calculation of different physical constants of heterogeneous substances: I. Dielectric constants and conductances of mixtures of isotropic substances). *Ann. Phys.*, **24**, 636–679.

Chen, J. and T. Tsai, 2016: Triple-Moment Modal Parameterization for the Adaptive Growth Habit of Pristine Ice Crystals. J. Atmos. Sci., 73, 2105–2122, https://doi.org/10.1175/JAS-D-15-0220.1

Chern, J.-D., W.-K. Tao, S. E. Lang, T. Matsui, J.-L. F. Li, K. I. Mohr, G. M. Skofronick-Jackson, *and* C. D. Peters-Lidard *(*2016*)*, Performance of the Goddard multiscale modeling framework with Goddard ice microphysical schemes, J. Adv. Model. Earth Syst., 7, *doi:*10.1002/2015MS000469.

Dawson, D.T., E.R. Mansell, Y. Jung, L.J. Wicker, M.R. Kumjian, and M. Xue, 2014: Low-Level ZDR Signatures in Supercell Forward Flanks: The Role of Size Sorting and Melting of Hail. *J. Atmos. Sci.*, **71**, 276–299, https://doi.org/10.1175/JAS-D-13-0118.1

Debye, P., 1929: Polar Molecules. The Chemical Catalog Company, New York.

Dolan, B., and S. A. Rutledge, 2009: A theory-based hydrometeor identification algorithm for Xband polarimetric radars. J. Oceanic Atmos. Technol., 46, 1196-1213, 10.1175/2009JTECHA1208.1.

Dolan, B., S. A. Rutledge, S. Lim, V. Chandrasekar, and M. Thurai, 2013: A robust C-Band hydrometeor identification algorithm and application to a long-term polarimetric radar dataset. J. Appl. Meteor. Climatol., 52, 2162–2186.

Fridlind, A. M. et al., 2012: A comparison of TWP-ICE observational data with cloud-resolving model results, J. Geophy. Res., 117, D05204doi:10.1029/2011JD016595.

Garrett, T. J., Yuter, S.E., Fallgatter, C*., Shkurko, K*., Rhodes, S. R. and Endries, J. L., 2015: Orientations and aspect ratios of falling snow. Geophys. Res. Lett., 42, 4617?4622, doi:10.1002/2015GL064040

Han, M., S. A. Braun, T. Matsui, C. R. Williams, 2013: Evaluation of cloud microphysics schemes in simulations of a winter storm using radar and radiometer measurements. *J. Geophys. Res. Atmos.,* 118, 1401-1419. doi:10.1002/jgrd.50115.

Harrington, J., K. Sulia, and H. Morrison, 2013a: A method for adaptive habit prediction in bulk microphysical models. Part I: Theoretical development. J. Atmos. Sci., 70, 349–364, doi:https://doi.org/10.1175/JAS-D-12-040.1.

Hashino, T. and G.J. Tripoli, 2011: The Spectral Ice Habit Prediction System (SHIPS). Part III: Description of the Ice Particle Model and the Habit-Dependent Aggregation Model. J. Atmos. Sci., 68, 1125–1141, https://doi.org/10.1175/2011JAS3666.1

Hendry, A., Y. Antar, and G. McCormick, 1987: On the relationship between the degree of preferred orientation in precipitation and dual-polarization radar echo characteristics. Radio Sci., **22**, 37 – 50.

Heymsfield, A.J., A. Bansemer, C. Schmitt, C. Twohy, and M.R. Poellot, 2004: Effective Ice Particle Densities Derived from Aircraft Data. *J. Atmos. Sci.,* **61**, 982–1003, https://doi.org/10.1175/1520-0469(2004)061<0982:EIPDDF>2.0.CO;2

Heymsfield, A.J., C. Schmitt, and A. Bansemer, 2010: Improved Representation of Ice Particle Masses Based on Observatinos in Natural Clouds, 67, 3303-3318,

Holt, A., 1984: Some factors affecting the remote sensing of rain by polarization diversity radar in the 3- to 35-GHz frequency range. *Radio Sci.*, **19**, 1399 – 1412.

Iguchi, T., T. Nakajima, A. Khain, K. Saito, T. Takemura, H. Okamoto, T. Nishizawa and W.-K. Tao (2012a), Evaluation of cloud microphysics in JMA-NHM simulations using bin or bulk microphysical schemes through comparison with cloud radar observations., J. Atmos. Sci., 69, 2566-2586, DOI: 10.1175/JAS-D-11-0213.1.

Iguchi T., T. Matsui, J. J. Shi, W.-K. Tao, A. P. Khain, A. Hou, R. Cifelli, A. Heymsfield, and A. Tokay (2012b), Numerical analysis using WRF-SBM for the cloud microphysical structures in the C3VP field campaign: Impacts of supercooled droplets and resultant riming on snow microphysics, Journal of Geophyiscal Research, 117, D23206, doi:10.1029/2012JD018101.

Iguchi, T., T. Matsui, A. Tokay, P. Kollias, and W.-K. Tao (2012c), Two distinct modes in one-day rainfall event during MC3E field campaign: Analyses of disdrometer observations and WRF-SBM simulation. Geophysical Research Letters, 39, L24805, doi:10.1029/2012GL053329.

Iguchi, T., T. Matsui, W.-K. Tao, A. Khain, V. Phillips, C. Kidd, T. L'Ecuyer, S. Braun, and A. Hou (2014) WRF-SBM simulations of melting layer structure in mixed-phase precipitation events observed during LPVEx. J. Appl. Meteor. Climatol., 53, 2710-2731, doi:10.1175/JAMC-D-13-0334.1.

Iguchi, T. and T. Matsui, 2018: Advances in clouds and precipitation modeling supported by remote sensing measurements. Remote Sensing of Clouds and Precipitation. C. Andronache (eds) Springer Remote Sensing/Photogrammetry. Springer, Cham, 257-277. doi:10.1007/978-3-319-72583-3_10.

Jamesen, A.R. 1989: The interpretation and meteorological application of radar backscatter amplitude ratios at linear polarizations. J. Atmos. Oceanic Technol., 6, 908–919.

Jung, Y., G. Zhang, and M. Xue, 2008a: Assimilation of Simulated Polarimetric Radar Data for a Convective Storm Using the Ensemble Kalman Filter. Part I: Observation Operators for Reflectivity and Polarimetric Variables. *Mon. Wea. Rev.*, **136**, 2228–2245, https://doi.org/10.1175/2007MWR2083.1

Jung, Y., M. Xue, G. Zhang, and J.M. Straka, 2008b: Assimilation of Simulated Polarimetric Radar Data for a Convective Storm Using the Ensemble Kalman Filter. Part II: Impact of Polarimetric Data on Storm Analysis. *Mon. Wea. Rev.*, **136**, 2246–2260, https://doi.org/10.1175/2007MWR2288.1

Jung, Y., M. Xue, and G. Zhang, 2010: Simulations of Polarimetric Radar Signatures of a Supercell Storm Using a Two-Moment Bulk Microphysics Scheme. *J. Appl. Meteor. Climatol.*, **49**, 146–163, https://doi.org/10.1175/2009JAMC2178.1

Keenan, T., 2003: Hydrometeor classification with C-band polarimetric radar. Aust. Meteor. Mag., 51, 23–31.

Khain, A. P., Ovtchinnikov, M., Pinsky, M., Pokrovsky, A. and Krugliak, H., 2000: Notes on the state-of-the-art numerical modeling of cloud microphysics, Atmos. Res., 55, 159-224, doi:10.1016/S0169-8095(00)00064-8.

Khain, A. P., D. Rosenfeld and A. Pokrovsky, 2005: Aerosol impact on the dynamics and microphysics of deep convective clouds. Q. J. Roy. Met. Soc., 131, 2639-2663.

Khain, A., A. Pokrovsky, D. Rosenfeld, U. Blahak, and A. Ryzhkov, 2011: The role of CCN in precipitation and hail in a mid-latitude storm as seen in simulations using a spectral (bin) microphysics model in a 2D dynamic frame, Atmos. Res., 99, 129–146, doi:10.1016/j.atmosres.2010.09.015.

Kidd, C. T. Matsui, J. Chern, K. Mohr, C. Kummerow, and D. Randall (2016): Global precipitation estimates from cross-track passive microwave observations using a physically-based retrieval scheme. Journal of Hydrometeorology, 17, 383–400. doi: http://dx.doi.org/10.1175/JHM-D-15-0051.1

Knight, N.C., 1986: Hailstone Shape Factor and Its Relation to Radar Interpretation of Hail. J. Climate Appl. Meteor., 25, 1956–1958, https://doi.org/10.1175/1520-0450(1986)025<1956:HSFAIR>2.0.CO;2

Knight, C.A. and N.C. Knight, 1970: The Falling Behavior of Hailstones. *J. Atmos. Sci.*, **27**, 672–681, https://doi.org/10.1175/1520-0469(1970)027<0672:TFBOH>2.0.CO;2

Kollias, P. and Tatarevic, A. 2017: User’s Guide CR-SIM SOFTWARE v 2.2 (http://www.meteo.mcgill.ca/~aleksandra/CR-SIM/crsim-UserGuide-v2.0.pdf)

Korolev, A. and G. Isaac, 2003: Roundness and Aspect Ratio of Particles in Ice Clouds. J. Atmos. Sci., 60, 1795–1808, https://doi.org/10.1175/1520-0469(2003)060<1795:RAAROP>2.0.CO;2

Kumjian, M.R. and O.P. Prat, 2014: The Impact of Raindrop Collisional Processes on the Polarimetric Radar Variables. J. Atmos. Sci., 71, 3052–3067, https://doi.org/10.1175/JAS-D-13-0357.1

Lang, S., Tao, W.-K., Cifelli, R., Olson, W., Halverson, J., Rutledge, S. and Simpson, J., 2007: Improving simulations of convective system from TRMM LBA: Easterly and Westerly regimes. J. Atmos. Sci., 64, 1141-1164.

Lang, S., W.-K. Tao, J.-D. Chern, D. Wu, and X. Li, 2014: Benefits of a 4th ice class in the simulated radar reflectivities of convective systems using a bulk microphysics scheme. J. Atmos. Sci. (in press) doi: http://dx.doi.org/10.1175/JAS-D-13-0330.1

Li, X., W.-K. Tao, T. Matsui, C. Liu, and H. Masunaga (2010), Improving a spectral bin microphysical scheme using long-term TRMM satellite observations. *Quarterly Journal of Royal Metrological Society,* 136(647), 382-399.

Lin, Y.-L., Farley, R. D. and Orville, H. D., 1983: Bulk parameterization of the snow field in a cloud model. J. Clim.ate Appl. Meteor., 22, 1065-1092.

Marshall, S. J., and W. M. K. Palmer (1948), The distribution of raindrops with size, J. Meteorol., 5, 165–166, doi:10.1175/1520-0469(1948)005<0165:TDORWS>2.0.CO;2.

Matrosov, S.Y., R.F. Reinking, R.A. Kropfli, and B.W. Bartram, 1996: Estimation of Ice Hydrometeor Types and Shapes from Radar Polarization Measurements. *J. Atmos.*

Oceanic Technol., **13**, 85–96, https://doi.org/10.1175/1520-0426(1996)013<0085:EOIHTA>2.0.CO;2

Matsui, T., X. Zeng, W.-K. Tao, H. Masunaga, W. Olson, and S. Lang (2009), Evaluation of long-term cloud-resolving model simulations using satellite radiance observations and multifrequency satellite simulators. *Journal of Atmospheric and Oceanic Technology*, 26, 1261-1274.

Matsui, T. T. Iguchi, X. Li, M. Han, W.-K. Tao, W. Petersen, T. L'Ecuyer, R. Meneghini, W. Olson, C. D. Kummerow, A. Y. Hou, M. R. Schwaller, E. F. Stocker, J. Kwiatkowski (2013), GPM satellite simulator over ground validation sites, *Bull. Amer. Meteor. Soc.*, 94, 1653–1660. doi: http://dx.doi.org/10.1175/BAMS-D-12-00160.1

Matsui, T., 2013: Chapter 12. Mesoscale Modeling and Satellite Simulator, Mesoscale Meteorological Modeling. 3rd Edition, R. A. Pielke Sr. Ed. Academic Press, 760 p, ISBN: 9780123852373.

Matsui, T., J. Santanello, J. J. Shi, W.-K. Tao, D. Wu, C. Peters-Lidard, E. Kemp, M. Chin, D. Starr, M. Sekiguchi, and F. Aires, 2014: Introducing multisensor satellite radiance-based evaluation for regional Earth System modeling, J. Geophys. Res., 119, 8450–8475, doi:10.1002/2013JD021424.

Matsui, T., J. Chern, W.-K. Tao, S. Lang, M. Satoh, T. Hashino, and T. Kubota (2016), On the land-ocean contrast of tropical convection and microphysics statistics derived from TRMM satellite signals and global storm-resolving models. *Journal of Hydrometeorology*, 17, 1425-1445. doi:10.1175/JHM-D-15-0111.1.

Maxwell Garnett, J. C., 1904: Colours in metal glasses and in metallic films. *Philos. Trans. Roy. Soc. London*, **A203**, 385–420.

Mohr, C. G., and L. J. Miller, 1983: CEDRIC – A software package for Cartesian space editing, synthesis and display of radar fields under interactive control. *Preprints, 21st Conf. On Radar Meteorology,* Boston, *Amer. Meteor. Soc.*, 569-574.

Park, H.-S., A. V. Ryzhkov, D. S. Zrnic, and K.-E. Kim, 2009: The hydrometeor classification algorithm for the polarimetric WSR-88D: Description and application to an MCS. Wea. Forecasting, 24, 730–748.

Phillips, V., A. Khain, A. Pokrovsky, 2007. The influence of melting on the dynamics and precipitation production in maritime and continental storm-clouds. J. Atmos. Sci., 64 (2), 338–359.

Phillips, V.T., A. Khain, N. Benmoshe, and E. Ilotoviz, 2014: Theory of Time-Dependent Freezing. Part I: Description of Scheme for Wet Growth of Hail. J. Atmos. Sci., 71, 4527–4557, https://doi.org/10.1175/JAS-D-13-0375.1

Phillips, V.T., A. Khain, N. Benmoshe, E. Ilotoviz, and A. Ryzhkov, 2015: Theory of Time-Dependent Freezing. Part II: Scheme for Freezing Raindrops and Simulations by a Cloud Model with Spectral Bin Microphysics. *J. Atmos. Sci.*, **72**, 262–286, https://doi.org/10.1175/JAS-D-13-0376.1

Pielke, R. A. (2013), Mesoscale Modeling and Satellite Simulator, *Mesoscale Meteorological Modeling. 3rd Edition*, *Academic Press*, 760 p, ISBN: 9780123852373.

Powell, S.W., R.A. Houze, and S.R. Brodzik, 2016: Rainfall-Type Categorization of Radar Echoes Using Polar Coordinate Reflectivity Data. *J. Atmos. Oceanic Technol.,* **33**, 523–538, https://doi.org/10.1175/JTECH-D-15-0135.1

Pruppacher, H. and J. Klett 1997, Microphysics of Clouds and Precipitation. Kluwer, 954 pp.

Putnam, B.J., M. Xue, Y. Jung, N. Snook, and G. Zhang, 2014: The Analysis and Prediction of Microphysical States and Polarimetric Radar Variables in a Mesoscale Convective System Using Double-Moment Microphysics, Multinetwork Radar Data, and the Ensemble Kalman Filter. Mon. Wea. Rev., 142, 141–162, https://doi.org/10.1175/MWR-D-13-00042.1

Putnam, B.J., M. Xue, Y. Jung, G. Zhang, and F. Kong, 2017: Simulation of Polarimetric Radar Variables from 2013 CAPS Spring Experiment Storm-Scale Ensemble Forecasts and Evaluation of Microphysics Schemes. Mon. Wea. Rev., 145, 49–73, https://doi.org/10.1175/MWR-D-15-0415.1

Rutledge, S. A. and Hobbs, P. V., 1984: The mesoscale and microscale structure and organization of clouds and precipitation in mid-latitude clouds. Part XII: A diagnostic modeling study of precipitation development in narrow cold frontal rainbands. J. Atmos. Sci., 41, 2949-2972.

Ryzhkov, A. V., 2007: The impact of beam broadening on the quality of radar polarimetric data. *Journal of Atmospheric and Oceanic Technology* 24.5: 729-744.

Ryzhkov, A**.**, D.S. Zrnic, J.C. Hubbert, V.N. Bringi, J. Vivekanandan, E.A. Brandes, 2002: Polarimetric radar observations and interpretation of co-cross-polar correlation coefficients. Journal of Atmospheric and Oceanic Technology, **19**, 340 - 354.

Ryzhkov, A., and D.S. Zrnic, 2007: Depolarization in ice crystals and its effect on radar polarimetric measurements. Journal of Atmospheric and Oceanic Technology, **24**, 1256 - 1267.

Ryzhkov, A., M. Pinsky, A. Pokrovsky, and A. Khain, 2011: Polarimetric Radar Observation Operator for a Cloud Model with Spectral Microphysics. J. Appl. Meteor. Climatol., 50, 873–894. doi: http://dx.doi.org/10.1175/2010JAMC2363.1

Ryzhkov, A.V., M.R. Kumjian, S.M. Ganson, and A.P. Khain, 2013: Polarimetric Radar Characteristics of Melting Hail. Part I: Theoretical Simulations Using Spectral Microphysical Modeling. J. Appl. Meteor. Climatol., 52, 2849–2870, https://doi.org/10.1175/JAMC-D-13-073.1.

Sachidananda, M., and D. S. Zrnic, 1985: ZDR measurement considerations for a fast scan capability radar. Radio Sci.,20, 907–922.

Schrom, R.S. and M.R. Kumjian, 2018: Bulk-Density Representations of Branched Planar Ice Crystals: Errors in the Polarimetric Radar Variables. *J. Appl. Meteor. Climatol.*, **57**, 333–346, https://doi.org/10.1175/JAMC-D-17-0114.1

Snyder, J.C., H.B. Bluestein, G. Zhang, and S.J. Frasier, 2010: Attenuation Correction and Hydrometeor Classification of High-Resolution, X-band, Dual-Polarized Mobile Radar Measurements in Severe Convective Storms. *J. Atmos. Oceanic Technol.,* **27**, 1979–2001, https://doi.org/10.1175/2010JTECHA1356.1

Snyder, J.C., H.B. Bluestein, D.T. Dawson II, and Y. Jung, 2017a: Simulations of Polarimetric, X-Band Radar Signatures in Supercells. Part I: Description of

Experiment and Simulated ρhv Rings. *J. Appl. Meteor. Climatol.,* **56**, 1977–1999, https://doi.org/10.1175/JAMC-D-16-0138.1

Snyder, J.C., H.B. Bluestein, D.T. Dawson II, and Y. Jung, 2017b: Simulations of Polarimetric, X-Band Radar Signatures in Supercells. Part II: ZDR Columns and Rings and KDP Columns. *J. Appl. Meteor. Climatol.*, **56**, 2001–2026, https://doi.org/10.1175/JAMC-D-16-0139.1

Shi, J. J., W.-K. Tao, T. Matsui, A. Hou, S. Lang, C. Peters-Lidard, G. Jackson, R. Cifelli, S. Rutledge, and W. Petersen (2010), Microphysical Properties of the January 20-22 2007 Snow Events over Canada: Comparison with in-situ and Satellite Observations. *Journal of Applied Meteorology and Climatology*. 49(11), 2246–2266.

Straka, J.M., D.S. Zrnić, and A.V. Ryzhkov, 2000: Bulk Hydrometeor Classification and Quantification Using Polarimetric Radar Data: Synthesis of Relations. *J. Appl. Meteor.,* **39**, 1341–1372, https://doi.org/10.1175/1520-0450(2000)039<1341:BHCAQU>2.0.CO;2

Sulia, K.J. and M.R. Kumjian, 2017: Simulated Polarimetric Fields of Ice Vapor Growth Using the Adaptive Habit Model. Part I: Large-Eddy Simulations. Mon. Wea. Rev., 145, 2281–2302, https://doi.org/10.1175/MWR-D-16-0061.1

Tao, W.-K., Moncrieff, M., 2009. Multi-scale cloud-system modeling. Reviews in Geophysics 47 (4), RG4002. http://dx.doi.org/10.1029/2008RG000276.

Tao, W.-K., Wu, D., Matsui, T., Peters-Lidard, C., Lang, S., Hou, A., Rienecker, M., Petersen, W., and Jensen, M., 2013: Precipitation intensity and variation during MC3E: A numerical modeling study, Journal of Geophysical Research, Atmosphere, 118(13), 7199-7218, doi:10.1002/jgrd.50410.

Tao, W.-K., D. Wu, S. Lang, J.-D. Chern, C. Peters-Lidard, A. Fridlind, *and* **T.** Matsui *(*2016*)*, High-resolution NU-WRF simulations of a deep convective-precipitation system during MC3E: Further improvements and comparisons between Goddard microphysics schemes and observations, J. Geophys. Res. Atmos., 121, 1278–1305, doi:10.1002/2015JD023986.

Vivekanandan, J. W. M. Adams, and V. N. Bringi, 1991: Rigorous Approach to Polarimetric Radar Modeling of Hydrometeor Orientation Distributions. J. Appl. Meteor., 30, 1053–1063. doi: http://dx.doi.org/10.1175/1520-0450(1991)030<1053:RATPRM>2.0.CO;2

Yuter, S. E., and Robert A. Houze Jr., 1995: Three-dimensional kinematic and microphysical evolution of Florida cumulonimbus. Part II: Frequency distributions of vertical velocity, reflectivity, and differential reflectivity. *Mon. Wea. Rev.*, **123.7**, 1941-1963.

Zhang, S.Q., T. Matsui, S. Cheung, M. Zupanski, and C. Peters-Lidard, 2017: Impact of assimilated precipitation-sensitive radiances on the NU-WRF simulation of the West African Monsoon, *Monthly Weather Review Mon. Wea. Rev.*, 145, 3881–3900, https://doi.org/10.1175/MWR-D-16-0389.1

Zrnić, D. S., V. M. Melnikov, and A. V. Ryzhkov, 2006: Correlation coefficients between horizontally and vertically polarized returns from ground clutter. *Journal of Atmospheric and Oceanic Technology* 23.3, 381-394.

Tables

	RY11	**PU17**	**MA18**
Liquid (cloud & Rain)	A_{xis} = 0.9951+0.0251*D-0.03644*D^2 +0.005303*D^3-0.0002492*D^4 [Brandes et al. 2011] Type: quasi-Gaussian (Θ_{mean}= 0°, σ=1°)		
Ice (column)	A_{xis} = 2.0 Type: random		
Ice (plate)	A_{xis} = 0.35 Type: quasi-Gaussian (Θ_{mean}= 0°, σ=10°)		
Ice (dendrite)	A_{xis} = 0.125 Type: quasi-Gaussian (Θ_{mean}= 0°, σ=10°)		
Snow aggregate	A_{xis} = 0.8 Type: quasi-Gaussian (Θ_{mean}= 0°, σ=40°)	A_{xis} = 0.75 Type: quasi-Gaussian (Θ_{mean}= 0°, σ=20°)	A_{xis} = 0.7 - 0.05D + 0.003D^2 Type: quasi-Gaussian (Θ_{mean}= 0°, σ=20°)
Graupel	A_{xis} =max(0.8, 1.-0.2*D) Type: quasi-Gaussian (Θ_{mean}= 0°, σ=40°)	A_{xis} = 0.75 Type: quasi-Gaussian (Θ_{mean}= 0°, σ=10°)	A_{xis} = 0.814 Type: quasi-Gaussian (Θ_{mean}= 20°, σ=42°)
Hail	A_{xis} max(0.8, 1.-0.2*D) Type: quasi-Gaussian (Θ_{mean}= 0°, σ=40°)	A_{xis} = 0.75 Type: quasi-Gaussian (Θ_{mean}= 0°, σ=10°)	A_{xis} = max(0.725, 0.897 - 0.0008D - 0.0002D^2) Type: quasi-Gaussian (Θ_{mean}= 90°, σ=40°)

Table 1. Differing assumptions used for particle axis ratio and orientation angle distributions from *Ryzhkov et al.* [2011] (RY11), *Putnam et al.* [2017] (PU17), and this study (MA18). For all three sets of assumptions, identical values for rain and ice crystals are used for simplification. In the 4ICE microphysics, randomly oriented needle-shaped ice crystals are assumed so that the ice crystal class has essentially no impact on Z_{dr} and K_{dp}. A_{xis} is the axis ratio, D the diameter (in mm), Θ_{mean} the mean orientation angle (in degrees), σ the standard deviation of the orientation angle distributions (in degrees); *max*() and *min*() are Fortran operators indicating the selection of the maximum and minimum of the pair, respectively.

Figure Captions

Figure 1. Scattering geometry of an oblate particle with a specific orientation direction ($\vec{N}$) within a cartesian coordinate (X, Y, and Z). $\overrightarrow{N'}_{XY}$ is the projection of $\overrightarrow{N'}$ on the X-Y plane. $\overrightarrow{N'}$and Z' are the projections of $\vec{N}$ and the Z axis on the polarization plane. V and H are the linear polarization base vectors. Adapted from *Vivekanandan et al.* [1991].

Figure 2. Time series of 2 km horizontal cross-section of horizontal reflectivity (dBZ) from CSAPR observations (left) and the WRF-SBM (middle) and WRF-4ICE (right) simulations. Note that the CASPR observations are plotted using physical distance (in km from radar instrument), while the simulations use a latitude-longitude projection.

Figure 3. horizontal cross-sections of CSAPR a) HID retrieval (shaded), b) reflectivity, c) differential reflectivity, d) specific differential phase, e) co-polar correlation coefficient, f) radial velocity and wind vectors at 2 km MSL at 21:48Z on 23 May 2011 over the Southern Great Plains. Thick red contours in the HID panel a) separate convective and stratiform precipitation regimes.

Figure 4. Same as Figure 2 except for POLARRIS-f C-band simulations using the WRF-SBM output from 00Z 24 May 2011 and MA18 assumptions. Wind vectors are derived directly from WRF.

Figure 5. Same as Figure 2 except for POLARRIS-f simulations using the WRF-4ICE output from 00Z 24 May 2011. Axis ratio and orientation angle assumptions follow MA18.

Figure 6. Vertical cross-sections of the CSAPR radar observations (Z, Z_{dr}, K_{dp}, ρ_{hv}) and retrievals (w, wind vectors and HIDs) corresponding to those shown in Fig. 2 but along an east-west line located 10 km north of the radar location.

Figure 7. East-west vertical cross-sections along the 36.876N latitude of a) the WRF-SBM-simulated CSAPR radar observables (Z, Z_{dr}, K_{dp}, ρ_{hv}) and retrievals (w, HIDs) corresponding to those shown in Fig. 3. Wind vectors are derived directly from WRF. b) Corresponding model-simulated hydrometeor mass concentrations [g/m^3] along the same latitude. Axis ratio and orientation angle assumptions follow MA18.

Figure 8. Same as Fig. 6, but for the WRF-4ICE simulation at a latitude of 36.05 N and corresponding to Fig. 4. Axis ratio and orientation angle assumptions follow MA18.

Figure 9. CFADs of differential reflectivity and differential phase speed for convective and stratiform regions from the CSAPR observations and the POLARRIS simulations based on three different assumptions using the WRF-SBM simulation.

Figure 10. Same as Figure 8 but derived from the WRF-4ICE simulation.

Figure 11. PSDs estimated from the Citation HVPS-3, DR09 polarimetric radar retrieval assumptions for 0.5 mm hr^{-1} and 0 mm hr^{-1}, WRF-SBM (SBM), and WRF-4ICE (4ice).

Figure 12. HID SFADs from the CSAPR observations (top row) and the POLARRIS simulations for three different assumptions using the WRF-SBM simulation. The convective portion is shown in the left column and the stratiform in the right.

Figure 13. Vertical profiles comparing HID fractions for snow, graupel (including high and low density graupel), and hail from observations and WRF-SBM and WRF-4ICE with three different assumptions.

Figure1.

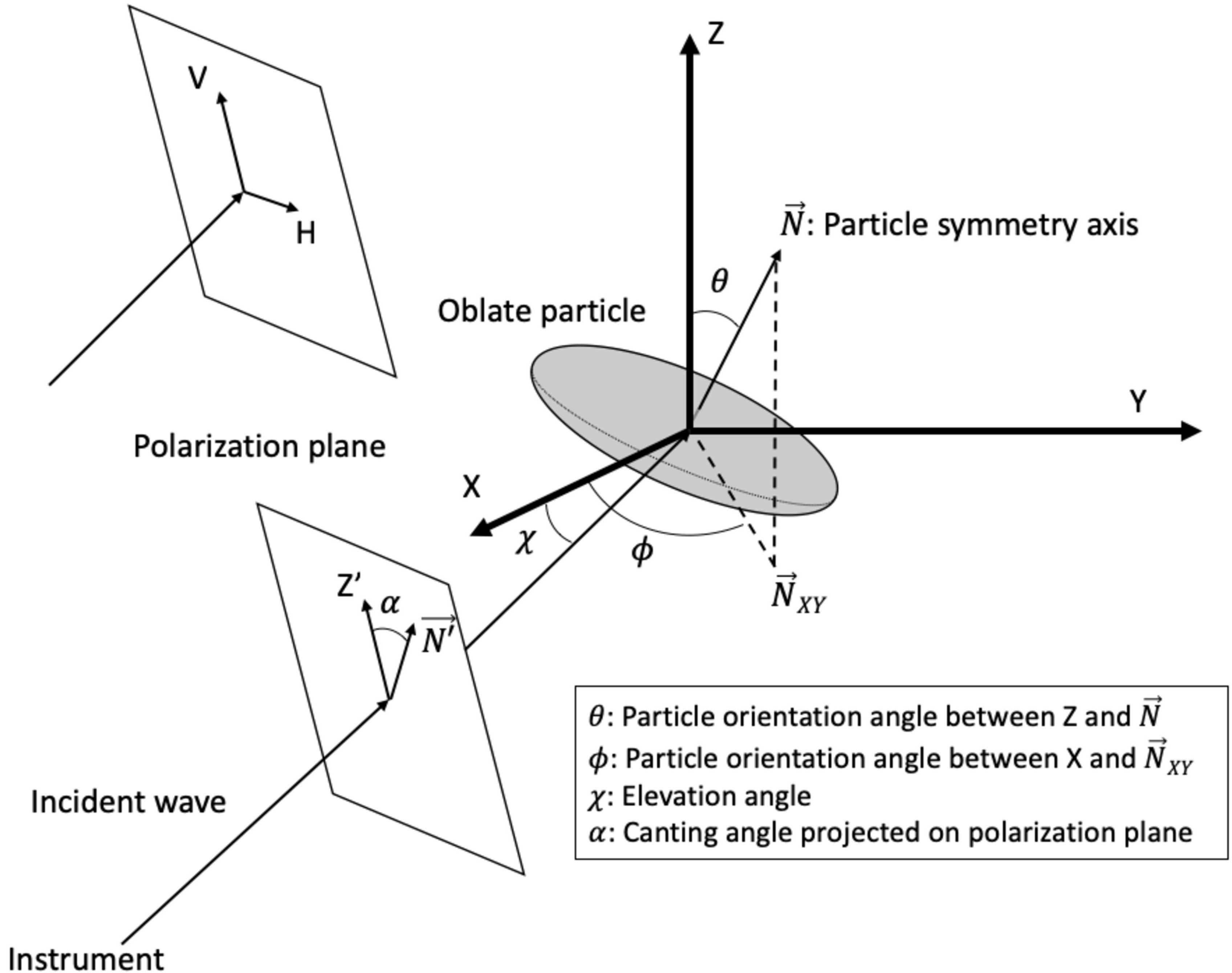

Z
V
H
$\vec{N}$: Particle symmetry axis
θ
Oblate particle
Y
Polarization plane
X
χ
ϕ
Z'
α
$\overrightarrow{N'}$
$\vec{N}_{XY}$
θ: Particle orientation angle between Z and $\vec{N}$
ϕ: Particle orientation angle between X and $\vec{N}_{XY}$
χ: Elevation angle
α: Canting angle projected on polarization plane
Incident wave
Instrument

Figure2.

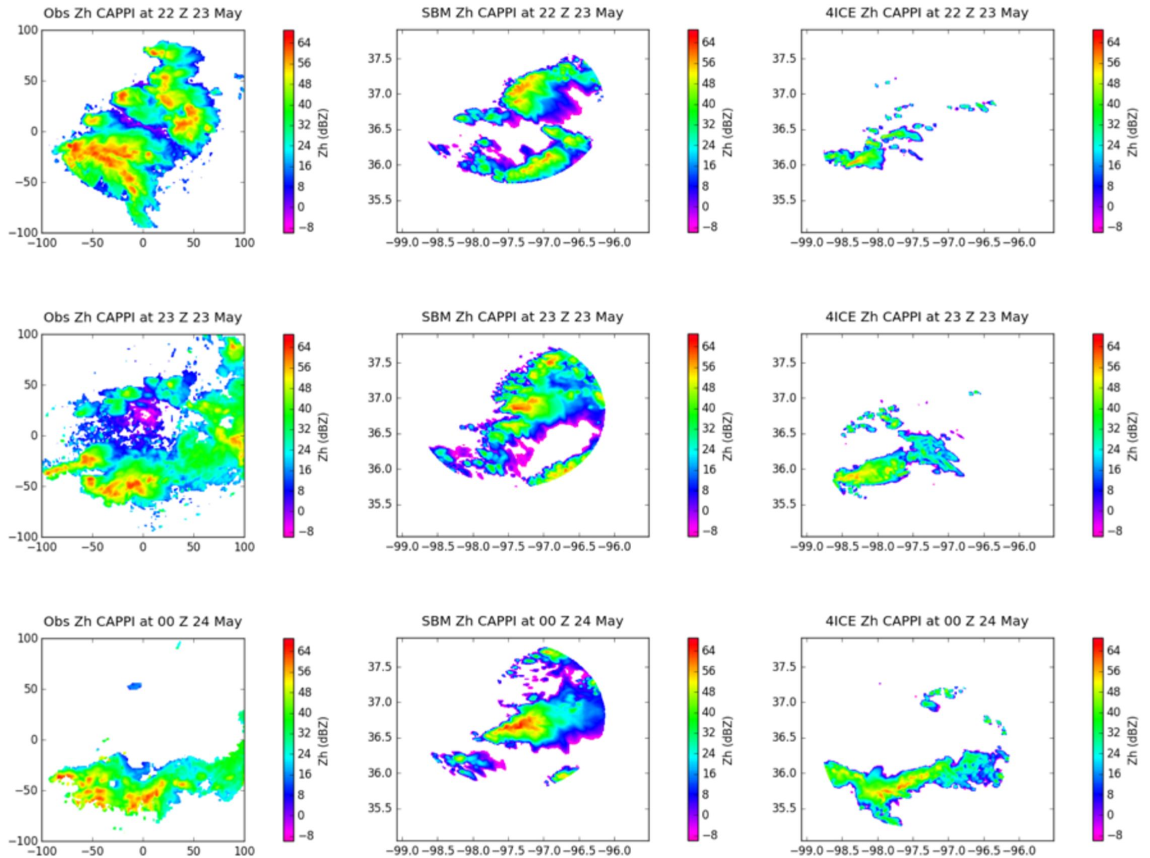
Obs Zh CAPPI at 22 Z 23 May
SBM Zh CAPPI at 22 Z 23 May
4ICE Zh CAPPI at 22 Z 23 May
Obs Zh CAPPI at 23 Z 23 May
SBM Zh CAPPI at 23 Z 23 May
4ICE Zh CAPPI at 23 Z 23 May
Obs Zh CAPPI at 00 Z 24 May
SBM Zh CAPPI at 00 Z 24 May
4ICE Zh CAPPI at 00 Z 24 May
Zh (dBZ)
−8 0 8 16 24 32 40 48 56 64
−100 −50 0 50 100
−99.0 −98.5 −98.0 −97.5 −97.0 −96.5 −96.0
35.5 36.0 36.5 37.0 37.5

Figure3.

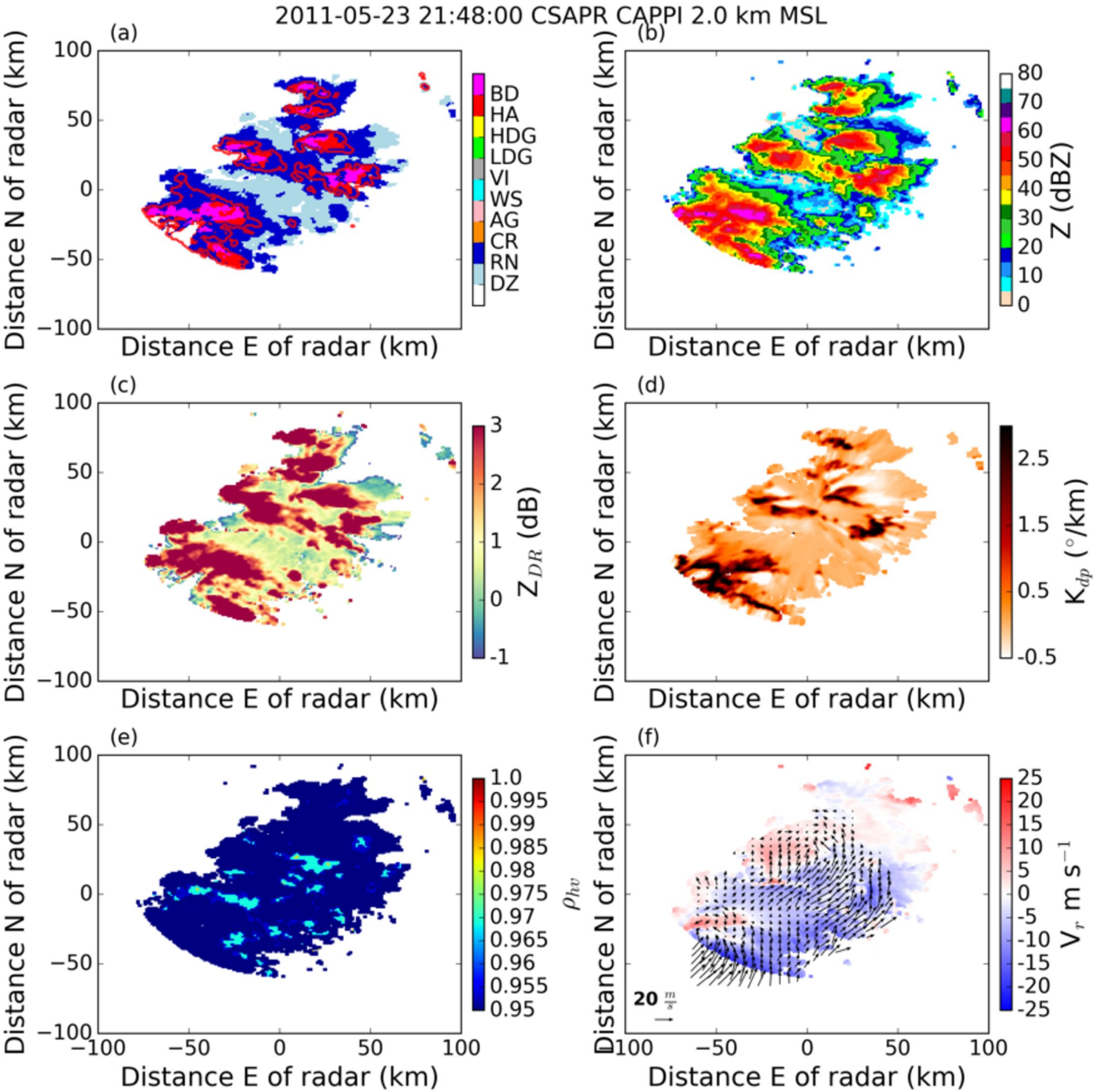
2011-05-23 21:48:00 CSAPR CAPPI 2.0 km MSL
(a)
(b)
(c)
(d)
(e)
(f)
BD
HA
HDG
LDG
VI
WS
AG
CR
RN
DZ
Z (dBZ)
Z_{DR} (dB)
K_{dp} (°/km)
ρ_{hv}
V_r m s^{-1}
20 $\frac{m}{s}$
Distance N of radar (km)
Distance E of radar (km)

Figure4.

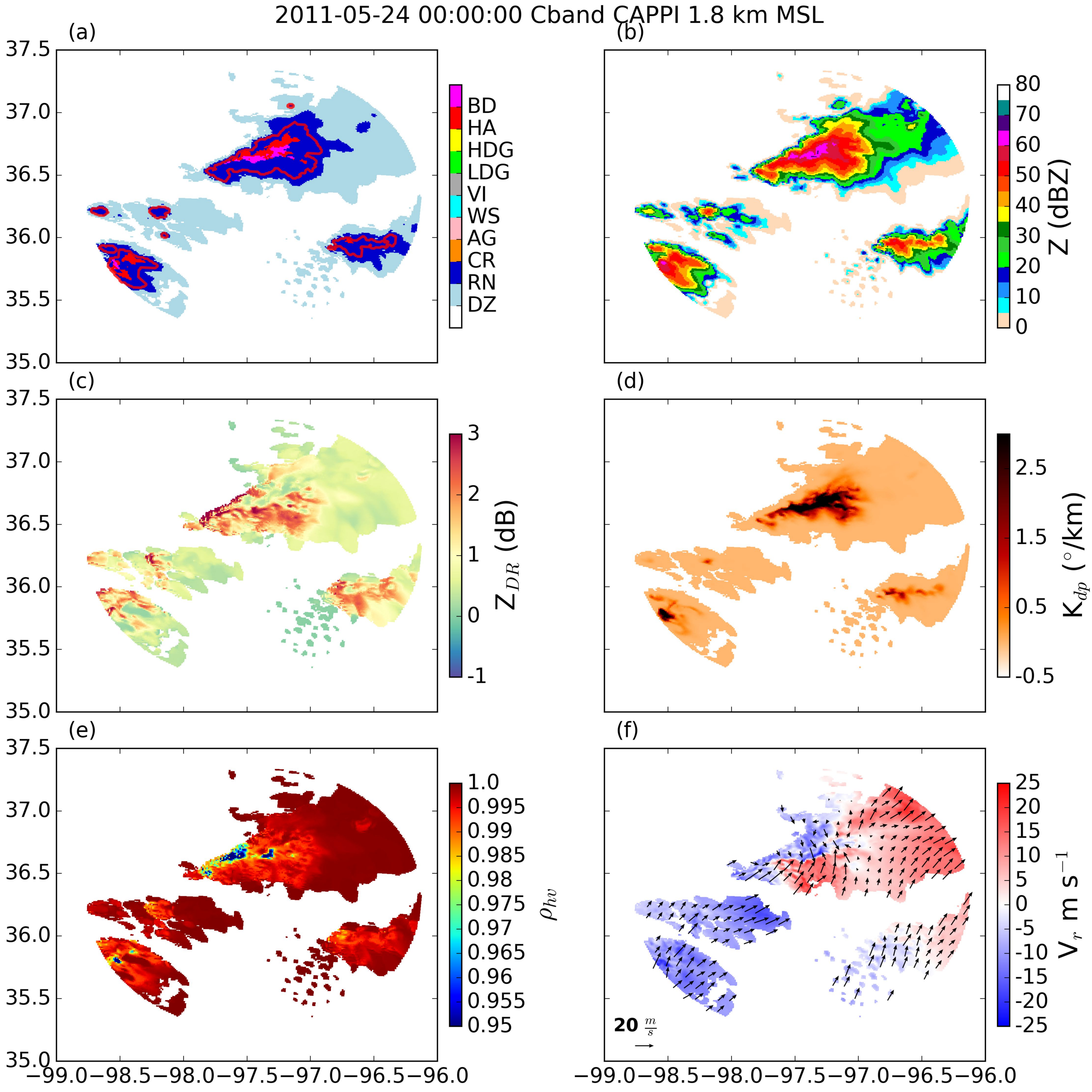

2011-05-24 00:00:00 Cband CAPPI 1.8 km MSL
(a)
(b)
(c)
(d)
(e)
(f)
BD
HA
HDG
LDG
VI
WS
AG
CR
RN
DZ
Z (dBZ)
Z_{DR} (dB)
K_{dp} (°/km)
ρ_{hv}
V_r m s^{-1}
20 $\frac{m}{s}$
37.5
37.0
36.5
36.0
35.5
35.0
−99.0
−98.5
−98.0
−97.5
−97.0
−96.5
−96.0

Figure5.

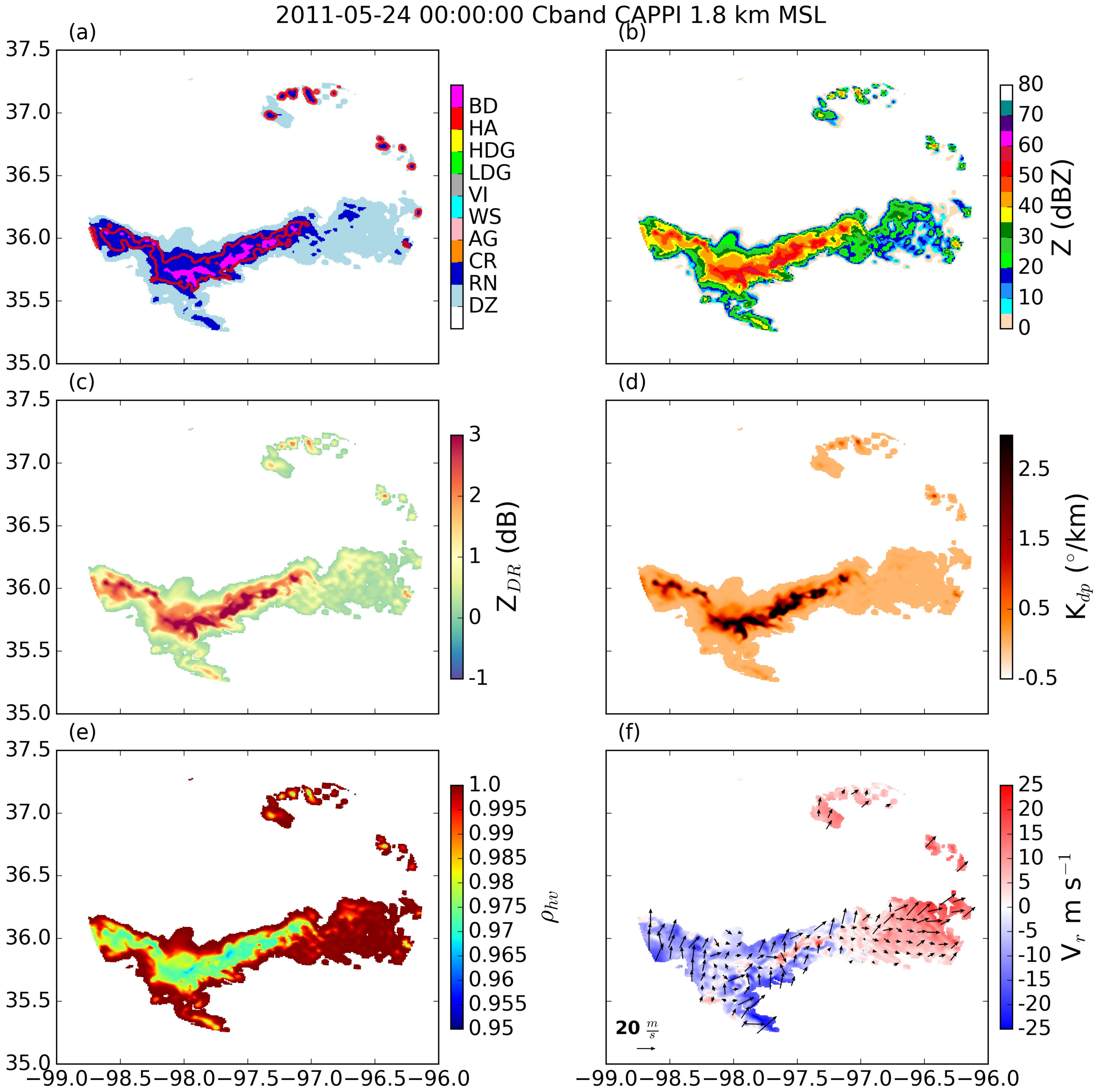
2011-05-24 00:00:00 Cband CAPPI 1.8 km MSL
(a)
(b)
(c)
(d)
(e)
(f)
BD
HA
HDG
LDG
VI
WS
AG
CR
RN
DZ
Z (dBZ)
Z_{DR} (dB)
K_{dp} ($^\circ$/km)
ρ_{hv}
V_r m s^{-1}
20 $\frac{m}{s}$
37.5
37.0
36.5
36.0
35.5
35.0
−99.0
−98.5
−98.0
−97.5
−97.0
−96.5
−96.0

Figure6.

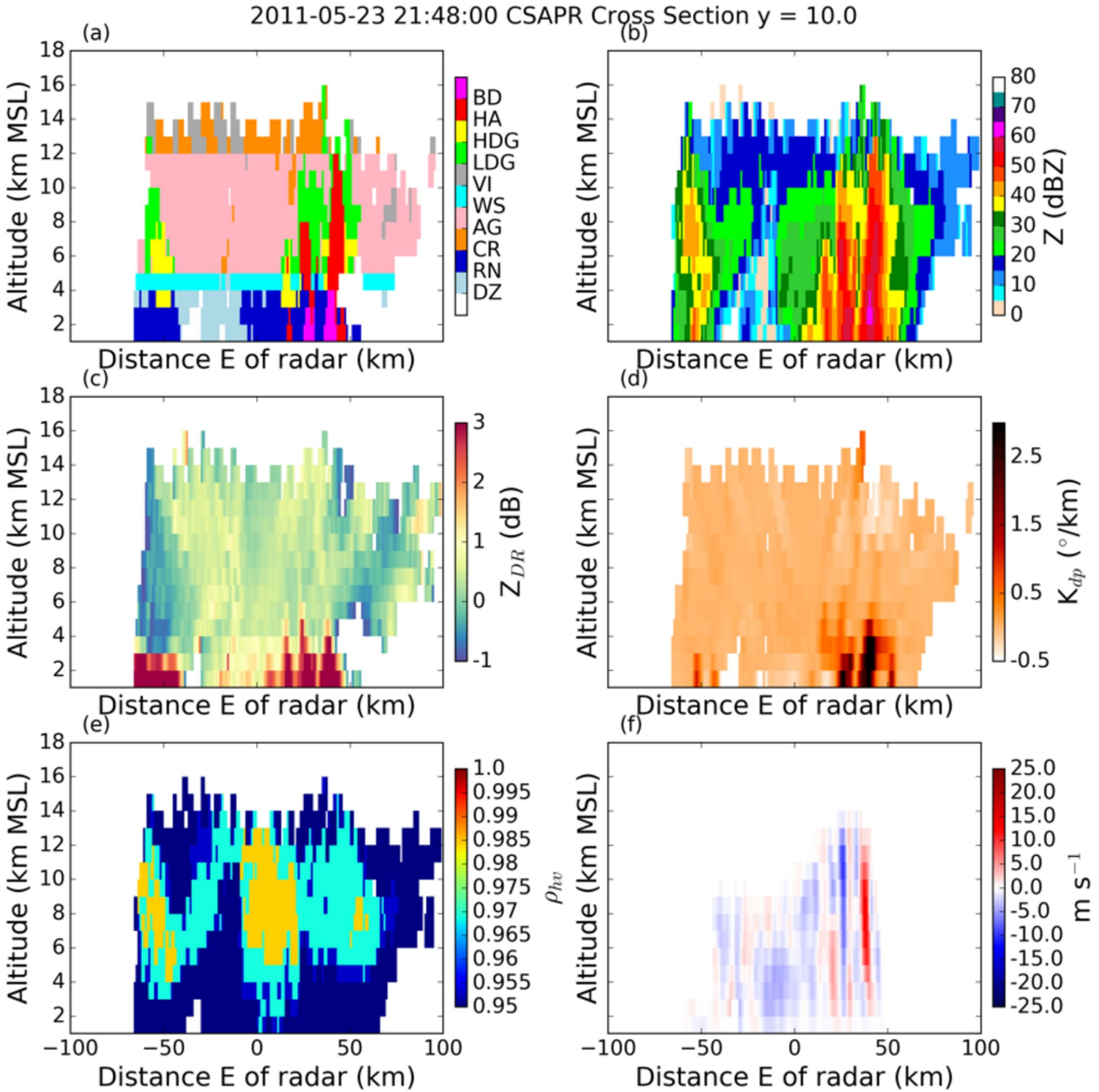
2011-05-23 21:48:00 CSAPR Cross Section y = 10.0
(a)
(b)
(c)
(d)
(e)
(f)
Altitude (km MSL)
Distance E of radar (km)
BD
HA
HDG
LDG
VI
WS
AG
CR
RN
DZ
Z (dBZ)
Z_{DR} (dB)
K_{dp} (°/km)
ρ_{hv}
m s^{-1}

Figure7.

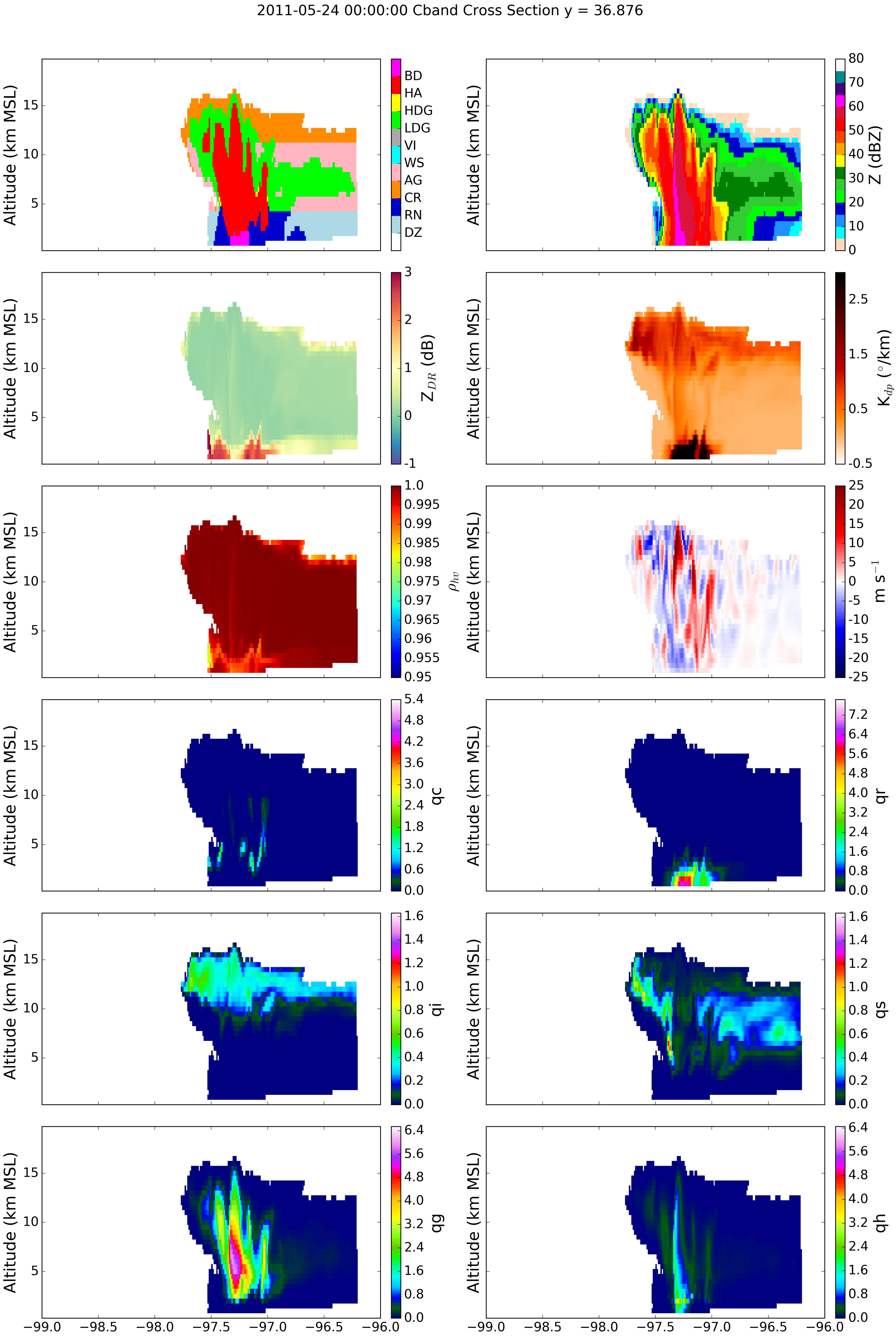
2011-05-24 00:00:00 Cband Cross Section y = 36.876
Altitude (km MSL)
BD
HA
HDG
LDG
VI
WS
AG
CR
RN
DZ
Z (dBZ)
Z_{DR} (dB)
K_{dp} (°/km)
ρ_{hv}
m s^{-1}
qc
qr
qi
qs
qg
qh
−99.0
−98.5
−98.0
−97.5
−97.0
−96.5
−96.0

Figure8.

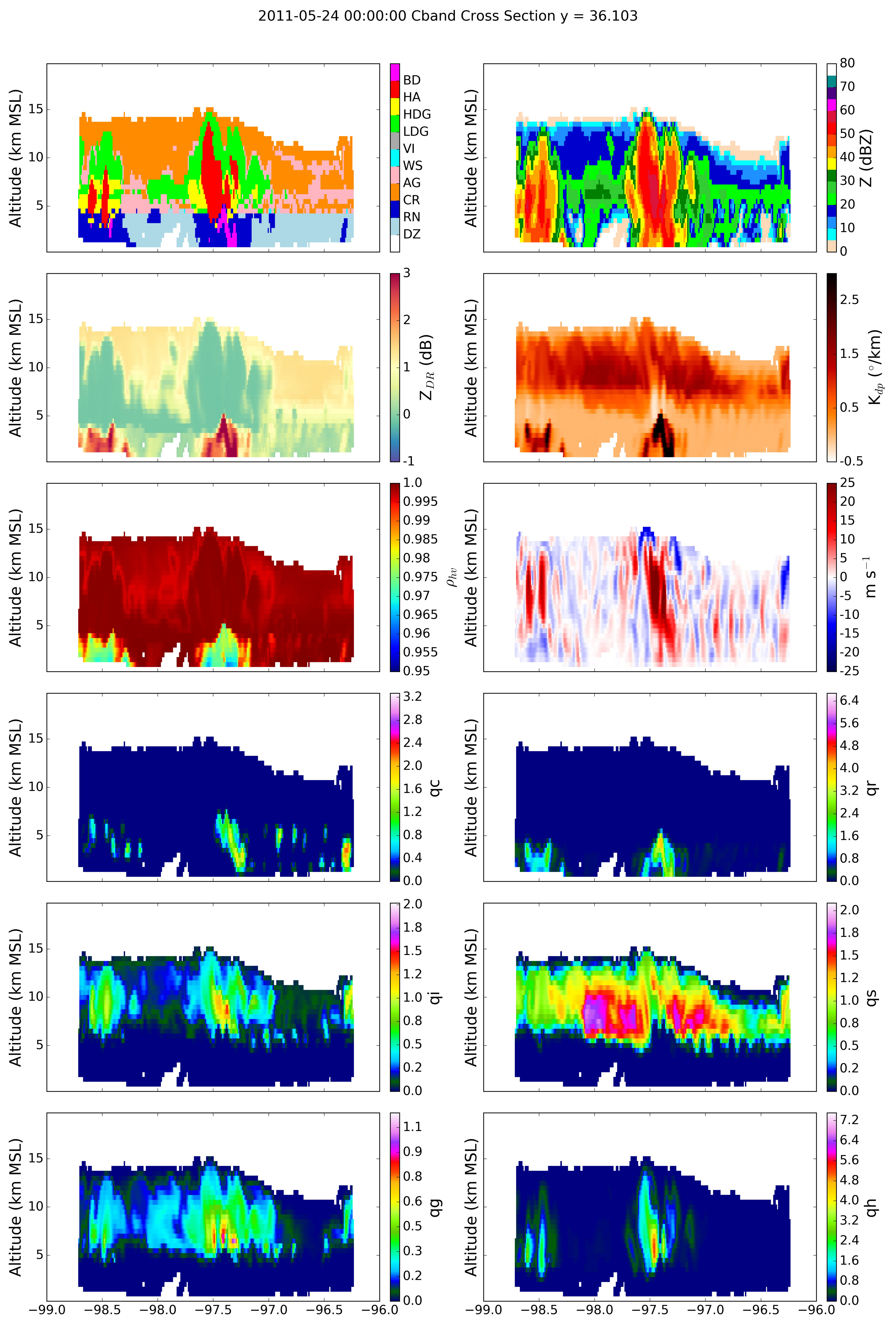

2011-05-24 00:00:00 Cband Cross Section y = 36.103
Altitude (km MSL)
BD
HA
HDG
LDG
VI
WS
AG
CR
RN
DZ
Z (dBZ)
Z_{DR} (dB)
K_{dp} (°/km)
ρ_{hv}
m s^{-1}
qc
qr
qi
qs
qg
qh

Figure9.

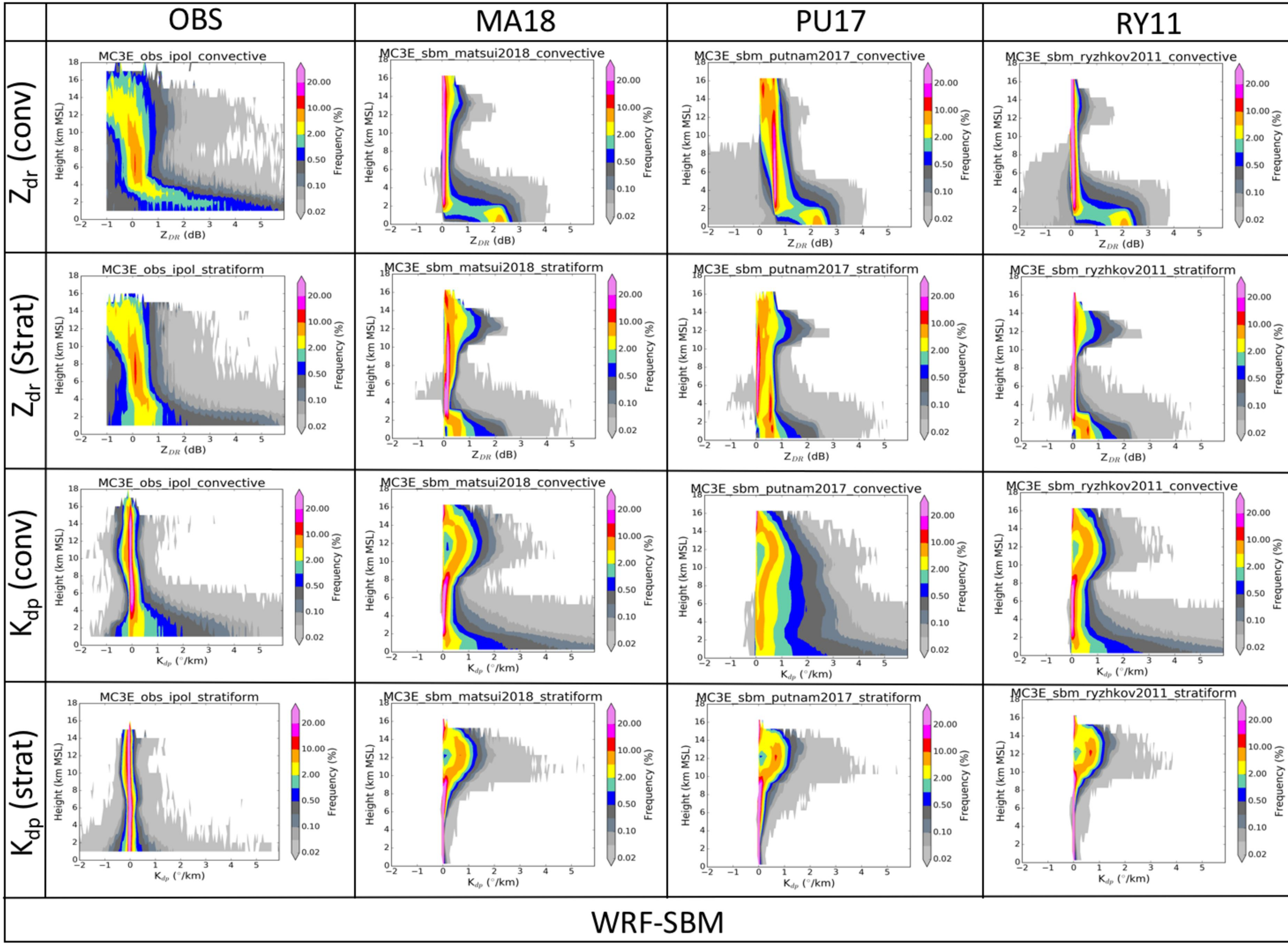

OBS
MA18
PU17
RY11
Z_{dr} (conv)
Z_{dr} (Strat)
K_{dp} (conv)
K_{dp} (strat)
MC3E_obs_ipol_convective
MC3E_sbm_matsui2018_convective
MC3E_sbm_putnam2017_convective
MC3E_sbm_ryzhkov2011_convective
MC3E_obs_ipol_stratiform
MC3E_sbm_matsui2018_stratiform
MC3E_sbm_putnam2017_stratiform
MC3E_sbm_ryzhkov2011_stratiform
Height (km MSL)
Z_{DR} (dB)
K_{dp} (°/km)
Frequency (%)
20.00
10.00
2.00
0.50
0.10
0.02
WRF-SBM

Figure10.

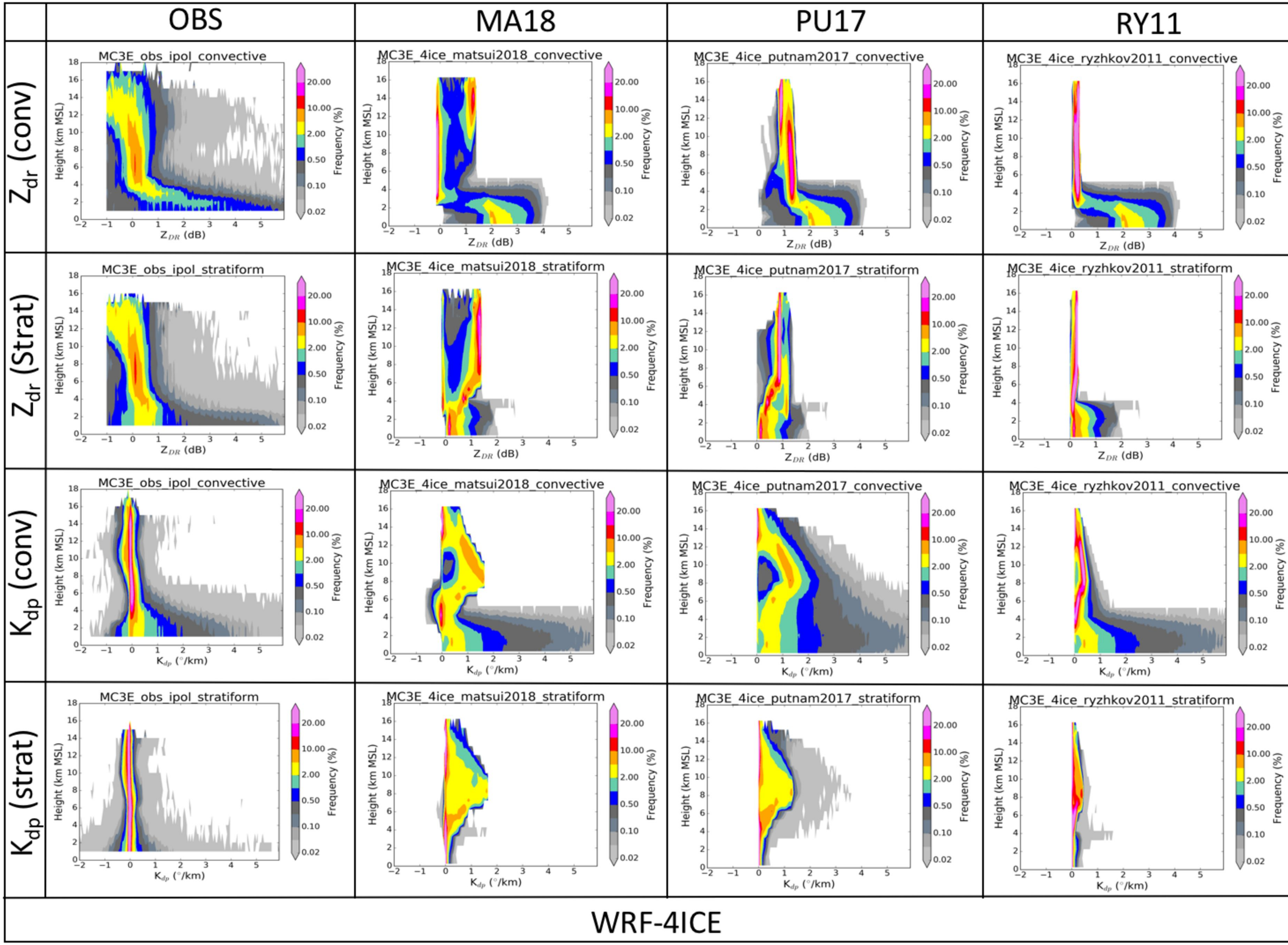
OBS
MA18
PU17
RY11
Zdr (conv)
Zdr (Strat)
Kdp (conv)
Kdp (strat)
MC3E_obs_ipol_convective
MC3E_4ice_matsui2018_convective
MC3E_4ice_putnam2017_convective
MC3E_4ice_ryzhkov2011_convective
MC3E_obs_ipol_stratiform
MC3E_4ice_matsui2018_stratiform
MC3E_4ice_putnam2017_stratiform
MC3E_4ice_ryzhkov2011_stratiform
Height (km MSL)
Z_DR (dB)
K_dp (°/km)
Frequency (%)
20.00
10.00
2.00
0.50
0.10
0.02
WRF-4ICE

Figure11.

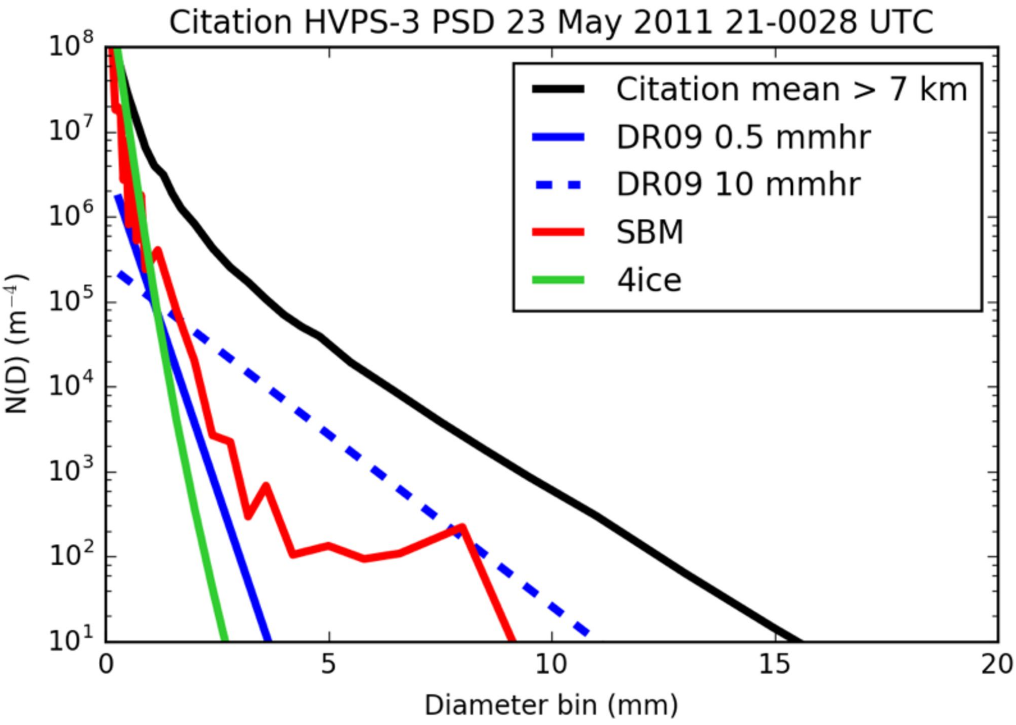

Citation HVPS-3 PSD 23 May 2011 21-0028 UTC
Citation mean > 7 km
DR09 0.5 mmhr
DR09 10 mmhr
SBM
4ice
N(D) (m^{-4})
Diameter bin (mm)
10^1
10^2
10^3
10^4
10^5
10^6
10^7
10^8
0
5
10
15
20

Figure12.

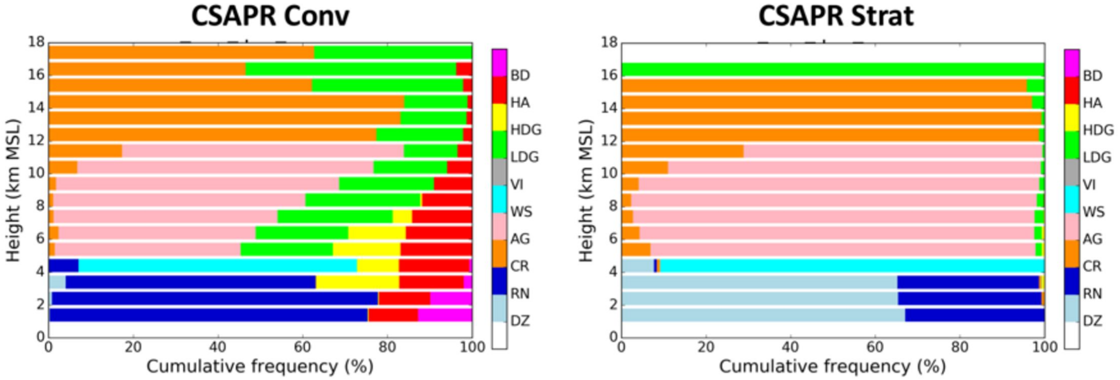
CSAPR Conv
CSAPR Strat
Height (km MSL)
Cumulative frequency (%)
BD
HA
HDG
LDG
VI
WS
AG
CR
RN
DZ

Figure13.

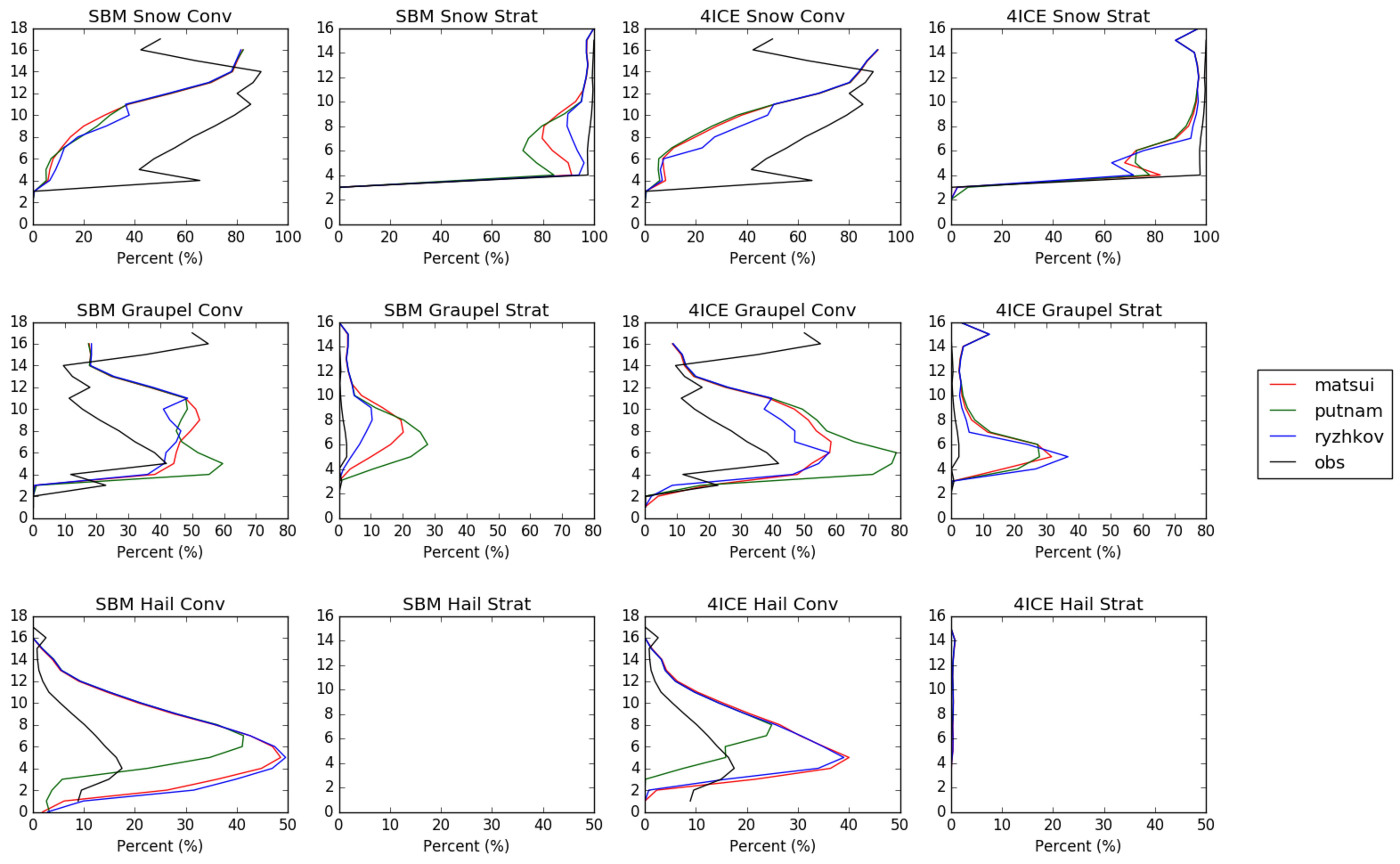

SBM Snow Conv
SBM Snow Strat
4ICE Snow Conv
4ICE Snow Strat
SBM Graupel Conv
SBM Graupel Strat
4ICE Graupel Conv
4ICE Graupel Strat
SBM Hail Conv
SBM Hail Strat
4ICE Hail Conv
4ICE Hail Strat
Percent (%)
matsui
putnam
ryzhkov
obs